Photon Counting Detectors for X-Ray Imaging With Emphasis on CT

R. Ballabriga, J. Alozy, F. N. Bandi, M. Campbell, *Member, IEEE*, N. Egidos, J. M. Fernandez-Tenllado, E. H. M. Heijne, *Life Fellow, IEEE*, I. Kremastiotis, X. Llopart, B. J. Madsen, D. Pennicard, V. Sriskaran, and L. Tlustos

***Abstract*—X-ray imaging is a widely used imaging modality in the medical diagnostic field due to its availability, low cost, high spatial resolution, and fast image acquisition. X-ray photons in standard X-ray sources are polychromatic. Detectors that allow to extract the "color" information of the individual X-rays can lead to contrast enhancement, improved material identification or reduction of beam hardening artifacts at the system level, if we compare them with the widely spread energy integrating detectors. Today, in the field of computed tomography (CT), prototypes of clinical grade systems based on spectral photon counting detectors are currently available for clinical research from different companies. One of the key system components in that development is the X-ray photon detector. This article reviews the photon detection hardware, from the conversion of X-rays into electrical signals to the pulse processing electronics. A review of available photon counting application specific integrated circuits (ASICs) for spectroscopic X-ray imaging is presented with emphasis on the CT medical imaging application.**

***Index Terms*—Application specific integrated circuits (ASICs), hybrid pixel detector, sensors.**

I. Introduction

X-RAYS have been used in the field of medicine since their discovery by Röntgen in 1895. They are helping radiologists and physicians to detect and characterize disease processes. Transmitted and detected X-ray beams generate a snapshot projection image, a series of projection images, or cross sectional tomographic images [1]. Developments in these techniques aim to improve the image quality and/or to reduce the required radiation dose to the patients. This can be achieved by improving the protocols, improving the hardware, and/or improving image reconstruction algorithms. Improving protocols involves optimizing the spectrum of the X-ray source for a given imaging task. Improving the hardware refers to optimizations in the X-ray generation and detection systems that allow to maximize the content of information from the X-ray beam impinging on the detector. This in turn leads to images optimized for the task. Improving algorithms involves processing the data from the detectors to reconstruct images maximizing the signal-to-noise ratio (SNR), for example. This article focuses on the detector optimization with emphasis on computed tomography (CT). Section II presents a classification of X-ray detectors depending on the type of photon conversion and on the approach taken to the processing of the detector signal. A summary of the status of energy sensitive photon counting detectors (PCDs) in CT is provided and the first results obtained with the technology are presented. Section III explains the physical processes in the sensor material and the imperfections in the readout electronics which limit the theoretical performance of photon counting technology. Section IV presents a review of readout application specific integrated circuits (ASICs) with photon counting signal processing. Section V focuses on aspects on the integration of the ASICs in a detector system and Section VI on the signal processing chain. Finally, a summary and conclusions (Section VII) is given.

Manuscript received February 15, 2020; revised May 9, 2020; accepted June 14, 2020. Date of publication June 16, 2020; date of current version July 2, 2021. *(Corresponding author: R. Ballabriga.)*

R. Ballabriga, J. Alozy, M. Campbell, N. Egidos, J. M. Fernandez-Tenllado, I. Kremastiotis, X. Llopart, B. J. Madsen, V. Sriskaran, and L. Tlustos are with Experimental Physics Department, CERN, 1211 Meyrin, Switzerland (e-mail: rafael.ballabriga@cern.ch).

F. N. Bandi is with CNM-IMSE, Parque Científico y Tecnológico Cartuja, 41092 Sevilla, Spain.

E. H. M. Heijne is with Experimental Physics Department, CERN, 1211 Meyrin, Switzerland, and also with IEAP CTU Prague, 110 00 Prague, Czech Republic.

D. Pennicard is with the Photon Science Detectors Group, DESY, 22607 Hamburg, Germany.

Color versions of one or more figures in this article are available at https://doi.org/10.1109/TRPMS.2020.3002949.

Digital Object Identifier 10.1109/TRPMS.2020.3002949

II. Detectors for X-Ray Imaging

X-ray detectors can be classified depending on how the signal of an X-ray photon is converted into an electrical signal. Detectors are classified into *indirect* and *direct* detection systems. In *indirect* detection systems the conversion of the X-ray photon into an electrical signal is done in two sequential processes: First the X-ray is converted into visible light by means of a segmented scintillator material. The individual scintillator pixels may be separated by a thin layer of septa to suppress optical crosstalk between adjacent elements. The amount of light generated is proportional to the energy of the incoming photon. Second, the light is detected and converted into an electrical signal in a segmented readout electronics containing photodiodes. The indirect conversion principle is shown in the drawing in Fig. 1(left).

In *direct* detection systems the X-ray photon deposits its energy, directly liberating electrical charges that drift to the collection electrodes under the influence of an electric field. The movement of the charges in the material induces an electrical current in the electrodes. For the X-ray energies used in

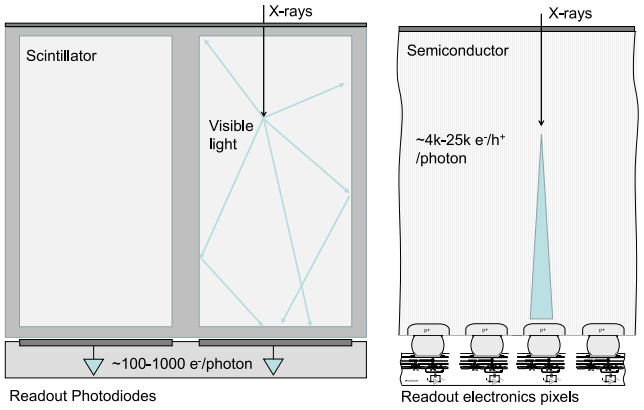

Fig. 1. Simplified scheme for the principle of operation of indirect detection (left) versus direct detection (right). (Plots not to scale.)

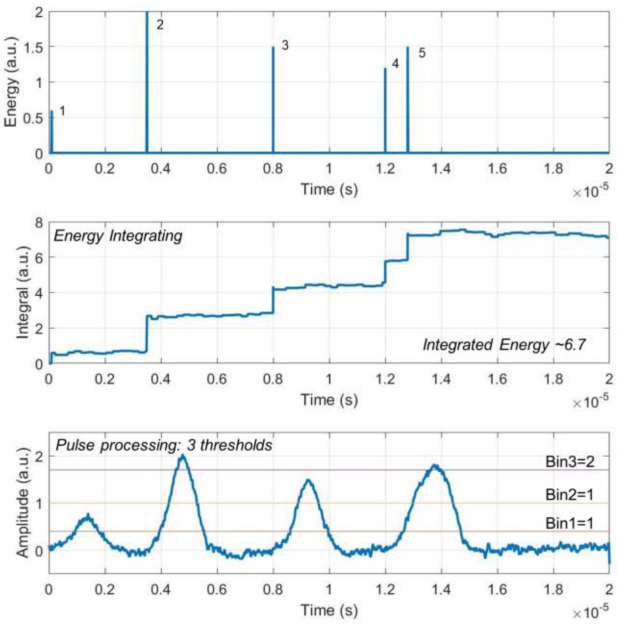

Fig. 2. Illustration of the operation of energy integrating (central plot) and pulse processing (bottom plot). The output of the analog electronics (before digitization) is shown. The impulses in the top plot illustrate the time of arrival of five photons to the detector. The amplitude of the impulses represents their energies (in arbitrary units). Photons 4 and 5 suffer from pile up in the pulse processing operation.

medical applications, each impinging photon releases a charge of between 4000 and 25 000 electrons in a CdTe semiconductor detector. The signal induced in the detector is highly reproducible. In an indirect conversion system the detected electrical signal is in the range from 100 to 1000 electrons depending on the scintillator characteristics. The concepts of indirect and direct conversion are illustrated in Fig. 1.

Another possible classification of X-ray detectors can be made depending on the type of signal processing architecture implemented in the readout electronics. In *integrating systems*, the signal deposited in the detector by the incoming photons is integrated over a given time exposure. The integral signal processing is illustrated in Fig. 2 (center plot). The integration process means that the information contained in the energy of the individual photon is lost. In integrating systems each photon contributes to the total signal with a weighting factor that is proportional to its energy. Higher energy photons thus contribute more to the signal than the lower energy ones. Moreover, noise sources such as dark current are included in the integral. This limits the SNR and the dynamic range of the system. The advantage of the integrating approach is the fact that the system can process photon events that arrive very close in time without degrading its functionality obtaining a linear response even at high fluxes.

In contrast to this approach, a *quantum imaging system,* also called *pulse processing system* or *photon counting system*, implements a readout architecture whereby the signal of each single X-ray photon is processed individually. The architecture usually consists of a charge sensitive amplifier (CSA) with pulse shaping followed by a group of discriminators and counters. When the signal deposited by a photon in the sensor is processed, a pulse develops at the output of the amplifier. The amplitude of this pulse is proportional to the detected charge. The discriminators compare this amplitude with a number of energy thresholds. A counter associated to an energy bin is incremented if the detected photon energy falls within this bin.

A signal is attributed to a photon only when it exceeds a threshold that is set above the intrinsic system noise and, in the ideal system, each converted photon is assigned to only one pixel [2]. This leads to suppression of false hits due to random electronics noise. As a consequence, the photon counting architecture permits the possibility of long acquisition time measurements with full electronics noise rejection. In this type of system, the impact of the random electronics noise is on the degradation of the energy resolution. Even though the energy threshold can guarantee full electronics noise rejection, its value may also cause a loss of detection efficiency, the loss increasing with the threshold level. The system has a perfect linear behavior over the entire dynamic range as long as the counter depth is sufficient and pulse pile up is avoided.

The operation of a readout channel in a pulse processing system is shown in Fig. 2 (bottom plot). The processing of the signal of a single photon by an electronic circuit with multiple energy thresholds leads to the possibility to acquire X-ray images whereby different sections of the incoming spectrum are sampled simultaneously. This is usually called spectral X-ray imaging.

One of the limitations of pulse processing systems, as can be seen in Fig. 2 (photon events 4 and 5) is the requirement of a minimum time between two consecutive photons to avoid their signals to overlap (which leads to a distortion in the measurement of the total number of detected photons and in their energies).

Most systems deployed today in medical X-ray imaging are indirect detection systems processed by integrating signal processing electronics. These are commonly known as energy integrating detectors (EIDs).

Dierickx *et al.* [3], [4] have investigated the approach of indirect detection systems read out by single pulse processing electronics.

There are also systems combining direct conversion with integrating signal processing. Detectors based on a-Se are commercially available and clinically used. The thickness of

the converter material is between 200 and 500 μm depending on the application. Each detector element has a capacitor which accumulates and stores the signal of the electrical charge and a thin film transistor (TFT) which serves as a switch. The readout of the charge in the capacitors is done on a row-by-row basis by closing the switch and sending the stored charge to a charge amplifier [5]. Figueras *et al.* [6] presented a prototype chip with 70-μm pixels bonded to a semiconductor detector material with charge integrating processing. This development is aimed at mammography. Dinapoli *et al.* [7] described a semiconductor readout ASIC with 25-μm pixel pitch for X-ray free electron laser (XFEL) applications in which a signal of up to $\sim 10^4$ photons can be simultaneously deposited on a single pixel within some femtoseconds.

There are two approaches to implement a PCD with direct detection [8]. The first approach is the *hybrid pixel detector* whereby each of the channels in a 2-D matrix of semiconductor sensor elements is connected to its own pulse processing circuit in a readout ASIC. The pixel pitch of the sensor element corresponds to the pitch of the readout channels in the ASIC. The connection is usually done with a fine-pitch flip-chip direct physical interconnection. The second approach is to read out the sensor elements by a dedicated ASIC whereby the pitch of the sensor pixel does not necessarily match the dimensions of the readout channel. The connection is done by means of an interposer or through the metal traces in a printed circuit board (PCB).

As already described above PCDs allow the allocation of photons from a polychromatic source into a plurality of energy bins. To optimize the image contrast-to-noise ratio (CNR), the largest weights can be applied to photons in the lower energy bins in which the contrast between tissues is highest [9]. PCDs also permit the identification of K-edges in contrast agents [1] enabling material identification without the need of kVp switching.

Today pulse-processing photon counting technology is available in different commercial products for medical imaging. The Lunar iDXA from GE is used in the medical environment for bone and metabolic health assessment. It contains a CdTe sensor read out by a pulse processing readout circuit [10]. Silicon strip detectors in an edge-on configuration are used in mammography [11].

In the past decade, there have been various developments to bring the photon counting technology to the field of CT. These developments cover many different areas, from sensor development, readout ASICs and image reconstruction algorithms [12].

A. Status of PCDs in Computed Tomography

Table I summarizes the main published developments going on in the field of PCDs in CT.

GE presented in [13] a study performed at the Rabin Medical Center in Israel. The system consisted of a VCT multislice system (LightSpeed VCT, GE, Milwaukee) assembled with DxRay's first generation PCD detector module [14]–[16]. The readout ASIC had been designed at CERN [17]. GE is currently collaborating with Stanford University, Rensselaer Polytechnic Institute (RPI) and University of Massachusetts Lowell on the research project high dose-efficiency CT. Detector modules have been integrated into a CT table-top system at RPI [18].

TABLE I
SUMMARY OF PCD PROJECTS IN THE FIELD OF CT

	Detector material	Detector thickness	Pixel cross section (mm)	ASIC Energy bins
GE Healthcare	CZT	2.5 mm	0.5 x 0.5	5
MBI	CdTe / CZT	2 mm	0.11 x 0.11	8
Philips	CZT	2 mm	0.5 x 0.5	5
KTH / Prismatic Sensors	Si	~3 cm	0.5 x 0.4	8
Siemens	CdTe	1.6 mm	0.225 x 0.225 (sub-pixel) / 0.9 x 0.9 (macropixel)	2 (Macromode) / 4 (Chess pattern mode)

MARS bio imaging (MBI) are collaborating with several universities in New Zealand (Canterbury, Otago, Lincoln, and Auckland), international research centers and commercial partners [19] to demonstrate applications of the PCD technology. Recent examples include quantifying targeted nanoparticles in bone microfractures [20], identifying suspected hemorrhage in atheroma [21], and differentiating crystals by chemical composition in gout [22]. First preclinical trials are ongoing [23]. They have installed Medipix3 readout chips connected to CZT converters in their scanners [24].

Philips presented in 2008 material separation studies with a preclinical spectral CT scanner equipped with a single line 1024-pixel CdTe detector with 6 energy thresholds [25]. Currently, Philips have developed a preclinical SPCCT prototype scanner (Philips Healthcare, Haifa, Israel) based on a clinical CT system (iCT, Philips Healthcare, Best, The Netherlands). The scanner is installed in Lyon, France [26]–[28] and has been recently upgraded to a 50 cm field-of-view scanner for human imaging. Philips are developing the ChromAIX family of hybrid pixel detector chips for the readout of CZT sensors [29], [30].

Prismatic Sensors is a company from Sweden that develops sensors for medical imaging based on silicon strip detectors. A feasibility study for this detector technology in CT was presented in [31]. Measurements with the silicon strip detectors have been performed in a Philips iCT gantry [32], [33]. A readout chip was developed for the readout of the strip segments [34].

Siemens built a research system based on the platform of a dual-source CT system. One source was coupled to an EID and the other to a photon-counting detector. There are prototype human-size scanners installed at the Mayo Clinic, National Institutes of Health and, Forchheim [35]. Siemens have developed different ASICs targeted to the CT application: the Actina chip developed in collaboration with CEA [36] and the MC1 [37].

B. First Results

The tests with PCDs in the CT application have shown that the technology allows to optimize the CNR compared to energy integrating detectors [9]. Energy weighting, i.e., applying larger (optimal) weights to photons in lower energies, becomes possible with PCDs.

Measurements in head CT scans presented by Pourmorteza *et al.* [38] have shown SNR of PCDs to be ∼20% higher than that of EIDs and up to a 30% improvement in gray matter-white matter CNR in noncontrast brain scans.

A reduction in image noise ∼20% for the application of lung nodule detection in chest CT has also been shown in [39].

Spatial resolution is typically also improved in PCDs compared to the ∼1-mm pitch EIDs. The availability of energy information allows to minimize beam hardening artifacts. The spatial resolution improvement and the minimization of beam hardening artifacts allows to accurately image metallic stents [40], [41].

Spectral photon counting CT has the potential for quantitative K-edge imaging, which has been demonstrated in both phantom and *in vivo* studies [42], [43]. With its potential to differentiate multiple contrast agents [42], photon counting CT will likely enable novel clinical applications, such as dual-contrast multiphase liver imaging within a single scan [44], differentiation between gadolinium enhanced polyps and iodine-tagged fecal material [27], and the visualization of the distribution of gold and iodine contrast media in different organs [45].

III. Radiation Detection Principles for PCDs

PCDs operate as solid-state ionization chambers. An X-ray photon that arrives at the detector has some probability to interact with it and deposit its energy (or a fraction of it) in the material volume. This probability is determined by the absorption efficiency. For typical photon energies used in medical X-ray imaging, there are two main interaction mechanisms: 1) the photoelectric effect and 2) Compton scattering.

In the case of the photoelectric effect, the photon ionizes an atom in the material from which an electron is ejected. This electron is usually called a photoelectron. The photoelectron interacts with the electrons in the surrounding detector atoms by means of inelastic Coulomb interactions moving them from the valence band to the conduction band, i.e., making them free to move in the material. The atom from which the photoelectron is ejected becomes in an excited state and it de-excites by ejecting either 1) a fluorescence photon or 2) an Auger Electron. When a fluorescence photon is emitted, it will leave the initial impact atom and may travel some distance away before depositing its energy or will even leave the material. When an Auger electron is emitted, it will interact with the electrons in the surrounding atoms by the same interaction mechanisms as the primary photoelectron.

In the case of Compton scattering, the incoming photon scatters inelastically transferring a fraction of its energy to an electron in the material. As in the case of fluorescence, the Compton scattered photon will deposit its remaining energy some distance away from the initial interaction point.

The deposition of energy from fluorescence and Compton scattered photons at a physical location different from the initial impact point will degrade the image quality. Moreover, the energy spectrum measured by a pixel will also be distorted due to 1) an incomplete charge collection in the illuminated pixel or 2) due to the crosstalk from signals in adjacent pixels (the fluorescence photons or Compton scattered photons from events taking place initially in neighboring pixels can be seen as a cross-talk).

The extent of the impact of these effects in the measured energy spectrum depends strongly on the converter selected for the application and on the detector geometry. Silicon is a low atomic number material ($Z = 14$ protons in the nucleus). When a photoelectric event takes place, the probability to generate a fluorescence photon (i.e., the fluorescence yield) is very small (∼4%) and the mean free path of these photons is relatively small (∼12 μm) compared to available pixel sizes. Cadmium Telluride is a compound semiconductor material made of Cadmium and Tellurium ($Z = 48$ and 52, respectively). The probability to generate fluorescence from photons above the respective K-edges in a photoelectric interaction is close to ∼85% for both materials and the mean free path for the fluorescence photons is ∼110 and ∼60 μm for the Cd and Te fluorescence photons, respectively. The high probability of occurrence of these photons and the long distance they can travel in the material without interacting means that they will have an impact in the form of a distortion in the measured pixel spectrum that has to be accounted for in the application and/or the signal processing.

In silicon, Compton scattering becomes the dominant interaction mechanism above ∼57 keV. In CdTe, on the other hand, the photoelectric effect is the dominant mechanism up to ∼265 keV [8].

If all the deposited energy of the incoming photon is contained in the detector volume, the number of electron-hole pairs generated by ionization (n) is proportional to the deposited energy by the photon (E_{ph}) and it depends on the detector material [i.e., $n = E_{ph}/\varepsilon$ where ε is the average energy to create an electron-hole pair, i.e., to move an electron from the valence to the conduction band, leaving a hole (vacancy) in the valence band]. (ε is larger than the semiconductor bandgap because energy is lost in other processes, e.g., lattice excitations).

An electric field applied to the material makes the free charge carriers drift toward the collection electrodes inducing a charge on them. The variation of this induced charge with time as the charge carriers move toward the electrodes results in an electrical current.

The induced current in the detector electrodes is calculated with the Shockley-Ramo theorem

$$i(t) = q\overrightarrow{v} \cdot \overrightarrow{E_w} \tag{1}$$

where q is the charge of the carrier, v is its drift velocity and E_w is the weighting field

$$\overrightarrow{v} = \mu\overrightarrow{E_d} \tag{2}$$

where μ is the carrier mobility and E_d is the drift field.

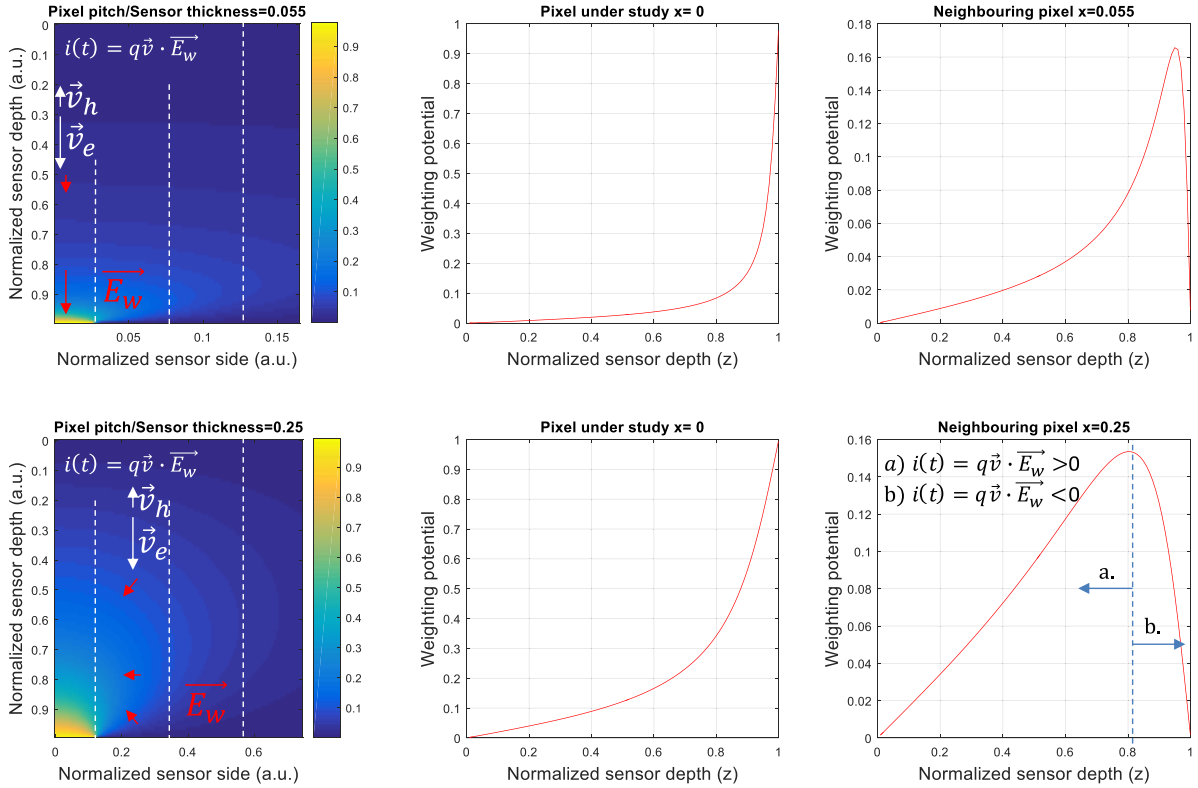

Fig. 3. Illustration of the calculation of the weighting potential for two different values of the pixel pitch to sensor thickness 0.055 (top plots) and 0.25 (bottom plots). The center plots correspond to the weighting potential along a path perpendicular to the plane of the pixel electrodes and centered in the pixel. The plots in the right correspond to the weighting potential along a path perpendicular to the plane of the pixel electrodes and centered in the center of the adjacent closest pixel.

The weighting field is defined as a potential that would exist in the detector with the electrode under study biased at unit potential while all other electrodes are at zero potential. The weighting field determines how a moving charge couples electrostatically to a specific terminal.

The induced charge is

$$Q = -q\Delta V_w = -q\big[V_w(x_f) - V_w(x_i)\big] \tag{3}$$

where ΔV_w is the difference in the weighting potential from the end of the path (the point in space where the carrier is collected) minus the origin (the point where the carrier is originated).

Fig. 3 illustrates the calculation of the induced charge for two different ratios of pixel pitch to sensor thickness. The top plot shows the case for a finely segmented detector with a pixel pitch to sensor thickness of 0.055 (that would be representative of a 2-mm CdTe sensor connected to a readout chip with 110-μm pixel pitch). The bottom plot shows a pixel pitch to sensor thickness of 0.25 (that would be representative of a 2-mm CdTe coupled to a readout chip with 500-μm pixels). The simulation was done from basic principles using the equations for the weighting potential presented in [46].

In the figure (left plots) the reader can see the weighting potential for a pixel with its center at $x = 0$. The gradient of the weighting potential is the weighting field (this is illustrated with red arrows). The weighting potential for the path of a charge carrier along the pixel center is shown in the center plots. By comparing the top (pitch/thickness $= 0.055$) with the bottom (pitch/thickness $= 0.25$) central plots, the reader can observe that, the gradient of the weighting potential in the vicinity of the pixel electrode is larger the smaller the pixel is with respect to the sensor thickness. From the central plots the reader can also infer (and quantify) that if a particle deposits its energy at a depth equidistant from the anode and the cathode (i.e., at $z = 0.5$) and the sensor is configured to collect electrons, the movement of the holes will contribute to $\sim$2.7% and $\sim$13% of the signal for the smaller and larger pixel pitch to sensor thickness, respectively. For the first case the electron drift contributes to 97.3% of the signal whereas in the second case (larger pitch) the electrons contribute to 87% of the induced charge. By making the pixel pitch to sensor thickness smaller, the contribution to the induced charge of the carrier that drifts toward the collection electrode is enhanced. This is known as the small pixel effect [47] and has also implications in the shape of the current pulse time-waveform at the input terminals of the readout electronics. Moreover, in the case of having very small pixels with respect to the sensor thickness, the gradient increases very close to the electrodes and as a consequence the induced current pulse is very short. For the same thickness, if the pixel pitch is larger, the induced current pulse is wider. If the amplifier's integration time is shorter than the time it takes for the induced charge to develop in the electrodes, then there is a loss of signal amplitude at the amplifier output due to incomplete charge collection. This is called *ballistic deficit*.

TABLE II
PHYSICAL PROPERTIES OF SEMICONDUCTORS USED AS RADIATION DETECTORS AT $T = 25\ ^{\circ}C$

Material	Si	Ge	GaAs	CdTe	CdZnTe	Perovskites ($MAPbI_3$) [a]	Perovskites ($CsPbBr_3$)
Atomic Number	14	32	31,33	48,52	48, 30, 52	66.8[b]	65.9[b]
Density (g/cm^3)	2.33	5.33	5.32	5.85	5.78	4.1	4.85
Band gap (eV)	1.12	0.67	1.43	1.44	1.57	1.51	2.28
Pair creation energy (eV)	3.62	2.96	4.2	4.43	4.6	4.63	3.3
Resistivity (Ω cm)	10^4	50	10^7	10^9	10^{10}	$>10^8$	10^9
$\mu_e\tau_e$ *(cm^2/V)*	>1	>1	$8\ 10^{-5}$	$3.3\ 10^{-3}$	$1\ 10^{-3}$	$>7\ 10^{-4}$	$>8\ 10^{-4}$
$\mu_h\tau_h$ *(cm^2/V)*	~1	>1	$4\ 10^{-6}$	$2\ 10^{-4}$	$3\ 10^{-4}$	$>8\ 10^{-4}$	$>1\ 10^{-3}$
μ_e *(cm^2/Vs)*	1400	3900	8000	1100	1000	70	-
μ_h *(cm^2/Vs)*	480	1900	4000	100	100	48	52

a. $MA^+=CH_3NH_3$
b. Effective atomic number.

In the plots in the right of Fig. 3, the weighting field along the path of a charge carrier in the center of the closest adjacent pixel is shown. Since the weighting potential is zero at both extremes, the total induced charge of the electrons and holes cancels. However, during the time the carriers drift toward the electrodes, a transient current signal will develop in the pixel input electrodes. This is illustrated in the bottom-left and bottom-right plots. If a photon deposits its energy in the center of the neighbor pixel, the current, i.e., the scalar product of the drift velocity by the weighting field, will change sign as the charge approaches the collection electrode (the change in the sign is illustrated in Fig. 3 with a dashed vertical line in the lower right plot). Therefore, the total induced charge in the neighbor pixel is zero. However, if the amplifier in the pixel is faster than the signal induction, a crosstalk signal may be detected.

In detector materials, there is some density of electron and hole trapping centers. Trapping leads to a loss of induced charge in the collection electrodes because those carriers which are trapped are prevented from contributing to the signal formation in the readout electrodes. This effect can be important in compound semiconductors or in radiation damaged Si sensors. The trapping length (L) is the mean distance travelled by the carrier before trapping or recombination. $L = t\mu E$ where t is the lifetime of the carrier, μ is the carrier mobility and E is the electric field. The mobility lifetime product is a key parameter describing the charge transport properties of a semiconductor. If we consider the electric field is constant inside the detector volume, $E = V/t$ (V is the sensor bias voltage and t is the sensor thickness) and the probability that the charge carrier recombines or is trapped is

$$P_{\text{loss}} = 1 - e^{-d/L} \tag{4}$$

where d is the distance for the carrier to travel to the detector electrodes.

Table II shows the physical properties of semiconductors typically used as radiation detectors. The values have been compiled from different sources [48]–[51]. For the mt product values in Table II for CdZnTe [50] (if $E = 300$ V/mm), the trapping length (L) is 30 and 9 mm for electrons and holes, respectively. When traveling 1 mm under the specified electric field, 3.28% of the electrons will be lost due to trapping or recombination whereas 10.5% of the holes will be lost when traveling the same distance. To minimize the impact of charge trapping, the designer can reduce the sensor thickness, increase the electric field strength or use material with higher mobility. The small pixel effect can also contribute to minimize the effects of charge trapping by reducing the contribution in the induced charge by the holes which are more susceptible to trapping.

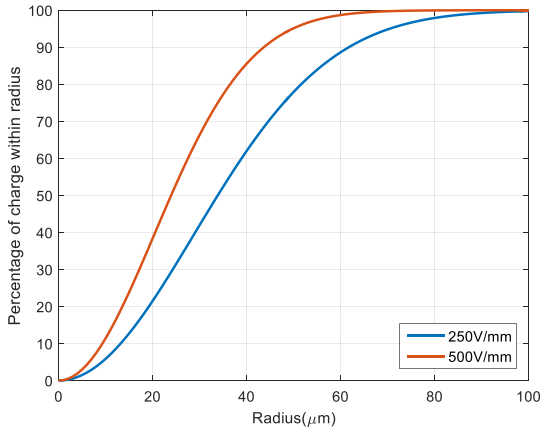

Fig. 4. Percentage of charge deposited within a given radius in a CdTe detector for a charge cloud traveling 2 mm, for different values of the electric field strength ($E = 250$ V/mm and $E = 500$ V/mm).

In addition to the movement of the charge carriers by drift, there is also a movement by diffusion, which causes the charge cloud to spread out as it travels toward the electrodes. The charge density distribution shows a cross section with a Gaussian distribution $\sigma = \text{sqrt}(2Dt)$ where D is the diffusion coefficient and t is the time it takes from the moment the energy is deposited to the moment the charge carriers are collected by the pixel electrodes.

The percentage of the charge that is collected within a given radius R has the expression

$$P_{\text{loss}} = 1 - e^{-\frac{qR^2E}{4KTd}} \tag{5}$$

where R is the radius of the charge cloud, E is the electric field q is the elementary charge, K is the Boltzmann constant, T is the temperature and d is the distance traveled by the carriers. Fig. 4 shows the percentage of charge deposited within a given radius for a 2-mm thick CdTe detector for two

different values of the electric field. For example, in the case of a 2-mm CdTe chip with an electric field of 250 V/mm, 90% of the charge generated shallow in the cathode will be deposited within a region delimited by a radius of 62 μm in the segmented anode (where the pixels collection electrodes are located). In the case of a 500-V/mm electric field, 90% of the charge is deposited within a radius of 44 μm. The extent of the impact of the charge diffusion has to be put in context with the dimensions of the pixels in a system.

When the photon interacts close to the edges or corners between adjacent pixels, the total induced charge in the detecting electronics is shared between those pixels. This is known as *charge sharing* due to diffusion. Charge sharing effects lead to distortion in the energy spectrum which is observed as a low energy tail. The impact of the distortion increases as the pixel pitch decreases with respect to the sensor thickness. The amount of charge sharing that occurs is dependent on the sensor bias voltage, as higher voltages imply shorter drift times.

As mentioned in previous paragraphs, increasing the bias voltage in the converter material has an impact on the signal generation in the pixel readout electrodes. It helps minimizing the impact of charge trapping by faster signal induction and minimizes the size of the charge cloud at the pixel electrodes due to charge diffusion. However, the optimal bias voltage for a real sensor depends on many parameters. As the voltage is increased (in absolute value), the leakage current increases and this leads to a degradation of the noise performance which leads to a degraded energy resolution. The extent of this degradation depends on the material and contact type. Sensors with ohmic contacts have higher leakage current increase with bias voltage with respect to sensors with blocking contacts. An excessive voltage can also lead to breakdown effects in the material. These effects are dependent not only on the bias voltage but also on the temperature and on the processing of the contact surfaces. If defects (e.g., point defects or grain boundaries) are present in the material, their behavior can be voltage-dependent and therefore, the optimal voltage for maximizing the sensor uniformity may be less than the maximum.

In Table II, apart from the traditional materials typically used as radiation detectors (Si [52], Ge [53], GaAs [54], [55], CdTe [30], and CdZnTe [56]) the authors have also included leaded halide perovskites, a material that is gaining some attention in the field of radiation detection [57], [58]. The reason is the strong stopping power [the material contains Pb ($Z = 82$)] and the fact that the crystal grows from a low cost solution. The cost of the materials for manufacturing single crystals is estimated by [59] to be less than 0.3 \$/cm^3. The spectrum of a ^{57}Co source has been measured and a resolution of 6.8% at 122 keV has been reported [51]. Although excellent performance has been demonstrated for these materials in solar cells, light emitting diodes and lasers, there are still outstanding challenges before their commercialization, e.g., long term stability of the crystal [59].

As already mentioned, the electronics circuit reading the signal from the sensor integrates the current signal on a capacitor, and shapes it producing a pulse with an amplitude proportional to the energy deposited by the photon in the pixel sensor volume. This amplitude is compared to different energy thresholds. The noise superimposed to the main signal from a photon event was illustrated in Fig. 2. This random signal is intrinsic to the electronics and has different origins [e.g., random thermal motion of charge carriers inside an electrical conductor (*thermal noise*), random fluctuations when a carrier flows across a potential barrier (*shot noise*) or effects of trapping/detrapping in the interfaces in MOS devices (*1/f noise*)].

Due to the stochastic nature of the photon arrival times there is some probability that two photons deposit their energy in the detector very close in time and as a consequence, their signals in the processing chain overlap. This is called pile-up and, at high flux rates, results in the distortion in the pulse amplitude measurement and in a subsequent loss of counts (also known as dead time losses). Analytical models have been presented for the dead time losses based on descriptions of the functionality implemented in the pulse processing electronics. The two models that are commonly used in the literature are the paralyzable and the nonparalyzable detector modes [60].

In the case of a nonparalyzable system the photon events arriving during the dead time of previous events are ignored and have no effect in the measurement. In the case of a paralyzable system, an event happening during the dead time of a first event is not accounted for in the total counts, and extends the dead time of the detecting channel by another dead time period (t) following the second occurrence. These represent simplified models of the full processing chain. A more accurate modeling of the front-end might be required to reproduce the results of a particular signal processing chain. An example is the semi-nonparalyzable model inferred in [61] to model the behavior of the processing in the ASIC [34].

Methods have been developed based on the properties of detectors to compensate for pile-up effects in the most demanding imaging modalities in terms of incoming flux [62], [63].

IV. Readout ASICs

A number of ASICs for the readout of semiconductor detectors for spectroscopic X-ray imaging have been designed by different groups. Some of the limiting factors intrinsic to direct-conversion radiation detectors presented in the previous sections have been addressed with ASIC implementations and system level solutions.

Table III presents the design parameters of photon counting hybrid pixel detector readout chips. The ASICs are sorted according to pixel size. The table contains information about different parameters: *Matrix* refers to the dimensions in number of pixels for the sensitive area of the chip. *Channel size* refers to the dimensions of the pixels in μm^2. *Energy thresholds* corresponds to the number of energy bins into which the incoming spectrum can be sampled. *Peaking time* corresponds to the time required for the shaper output to rise from zero to its maximum, the maximum value being proportional to the energy deposited by the incoming photon in the sensor volume associated to the pixel.

TABLE III
HYBRID PIXEL DETECTOR PHOTON COUNTING CHIPS

Name	Matrix	Channel size (μm^2)	Energy thresholds	Peaking time (ns)	Buttable sides	Tech. node	Specific information	Ref.
FRIC (AGH) (1)	64 x 64	50 x 50	2	10	1	40 nm	Prototype chip, 2x16 bit counters, 1.05V supply voltage. 2 modes of operation: 1. High Speed and 2. High Gain	[70]
Medipix3 (2),(3)	256 x 256	55 x 55	2	120	3	130 nm	Fine Pitch mode (55μm); (1) Single Pixel Mode (SPM), (2) Charge Sharing Correction Mode (CSM); ASIC is compatible with Through Silicon Vias technology (TSVs)	[71],[52]
Timepix3 (4)	256 x 256	55 x 55	10 bits	30	3	130 nm	Data push mode; event-by-event energy and time measurement; Charge Sharing Correction possible off-chip	[72]
Pixirad Pixie II (5)	512 x 476	52 x 60	2	300	2	180 nm	Hexagonal pixels, equivalent pixel pitch of 55.6μm	[73]
Samsung PC (6)	128 x 128	60 x 60	3	NS	0	130 nm	On-pixel successive approximation Analog to Digital Converter (ADC)	[74]
Pixirad Pixie III (7)	512 x 402	62 x 62	2	125	2	160 nm	Large area ASIC (31.7x25mm^2), Charge Sharing Correction algorithm	[75]
Eiger (8)	256 x 256	75 x 75	1	30	3	250 nm	Radiation hard electronics design	[68],[76]
PXD23K (AGH) (9)	128 x 184	75 x 75	2	48	3	130 nm		[77]
IBEX (Dectris) (10),(11)	256 x 256	75 x 75	2	NS	3	110 nm	Radiation hard electronics design; (10) Instant Retrigger technology, (11) Paralyzable operation	[64]
UFXC32K (12)	128 x 256	75 x 75	2	40	3	130 nm		[78]
LNPIX (13)	128 x 176	75 x 75	2	100	3	130 nm	Designed mainly for synchrotron applications; 2x14 bit counters/pixel up to 70k frames per second (2 bit/pixel)	[79]
X-Counter PC (14)	256 x 256	100 x 100	2	NS	3	NS	Charge Sharing Correction algorithm	[80], [81]
PXD18K (AGH) (15)	96 x 192	100 x 100	2	30	3	180 nm		[82]
FPDR90 (AGH) (16)	40 x 32	100 x 100	2	28	3	90 nm	Prototype ASIC	[83]
AGH_Fermilab (17)	18 x 24	100 x 100	2	48	0	40 nm	Prototype ASIC, Charge Sharing Correction algorithm	[84]
PXF40 (18)	18 x 24	100 x 100	1	8	0	40 nm	Prototype ASIC	[85]
Tsinghua PC (19)	32 x 32	100 x 100	2	100	3	180 nm		[86]
Medipix3 (20),(21)	128 x 128	110 x 110	8	120	3	130 nm	Spectroscopic mode (110μm pixels); (20) Single Pixel mode, (21) Charge Sharing Correction Algorithm; Compatible with TSVs	[71],[52]
XPAD3 (22)	80 x 120	130 x 130	2	150	3	250 nm		[87], [88]
HEPS-BPIX (23)	104 x 72	150 x 150	1	20	3	130 nm	ASIC mainly designed for synchrotron applications	[89], [90]
Pilatus 2 (24)	60 x 97	172 x 172	1	110	3	250 nm	Radiation hard electronics design	[91][92]
Pilatus 3 (25),(26)	60 x 97	172 x 172	1	110	3	250 nm	Radiation hard design; (25) Instant retrigger technology, (26) paralyzable model	[65]
Telesystems (27)	40 x 40	200 x 200	4	300-500	3	250 nm		[93]
Dosepix (28)	16 x 16	220 x 220	16	300	3	130 nm	On pixel energy binning with 16 programmable digital thresholds	[94]
Actina (CEA Siemens) (29)	64 x 64	225 x 225	2	20	3	NS	ASIC used in pre-clinical prototype systems. Supports pile-up trigger method.	[95][36][69]
Hexitec (30)	80 x 80	250 x 250	14 bits	2000	3	350 nm	Digitization of pulse amplitude off-chip with 14 bit ADC; ASIC compatible with TSVs	[56]
MC1 (Siemens) (31)	32 x 32	250 x 250	4	NS	4	NS	Chip can be tiled on 4 sides seamlessly. ASIC pixel layout is designed to match the geometry of the antiscatter grid	[37]
D2R1 (32)	16 x 16	300 x 300	13 bits	NS	2	180 nm	Triggered readout, Multi Correlated Double Sampling (MCDS)	[96]
ERICA (33)	8 x 20	330 x 330	6	100	3	250 nm	Digital Charge Sharing Correction Algorithm	[97]
CIX 0.2 (34)	8 x 8	500 x 250	1	NS	1	350 nm	Simultaneous charge integration and photon counting measurement	[98][99]
Philips ChromAIX1 (35)	16 x 16	300 x 300	4	20	2	180 nm		[29]
Ajat-0.35 (PC) (36)	32 x 64	350 x 350	1	1000	3	350 nm		[100],[101]
Ajat-0.35 (ADC) (37)	32 x 64	350 x 350	64	1000	3	350 nm	On-pixel ADC	[100],[101]
DxRay-Interon (38)	16 x 16	500 x 500	4	10	NS	NS		[102][103]
Ajat-0.5 (39)	44 x 22	500 x 500	2	1000-2000	3	350 nm		[104]
Philips ChromAIX2 (40)	22 x 32	500 x 500	5	10	3	180 nm		[30]
CEA-MultiX (41)	4 x 8	756 x 800	8 bits	NS	2	130 nm	On-pixel SAR ADC. Charge sharing, charge induction and pile-up correction	[105][106]

The indexes (in italics and inside curly brackets) in the table identify the chips in the following plots (they should not be confused with the references).

The electronics in hybrid pixel detectors is traditionally laid out in two regions. The first is the sensitive pixel matrix and the second is usually named the chip periphery, which contains circuitry to bias analog circuits in the pixels and digital circuitry to configure the chip and read out the measured information. The layout configuration of these two regions determines the number of sides on which the readout chips can be tiled seamlessly. This number is indicated in the table as *buttable sides*.

Technology node indicates the minimum feature size of the complementary metal-oxide semiconductor (CMOS) technological in which the ASICs were designed. The smaller feature sizes permit smaller transistors which are often faster and more power efficient for digital circuits.

The column indicated as *specific information* emphasizes characteristic features of the chips.

Table V presents photon counting semiconductor readout ASICs that are not hybridized to the sensor and, as

TABLE IV
ELECTRICAL PARAMETERS FOR HYBRID PIXEL DETECTOR PHOTON COUNTING CHIPS

Name	Max input count rate (Mcps/pixel)	Max input count rate (Mcps/mm^2)	10% count rate deviation (Mcps/mm^2)	Dead time (ns)	Electronics noise (e^- r.m.s.)	Energy resolution (FWHM)	Power/pixel (μW)
FRIC (AGH) (1)	8.5	1520	888	50 (High Speed Mode)	90	0.71 keV @ 8 keV, Si (High Gain) 1.13 keV @ 8 keV, Si (High Speed)	12 (High Gain) 18 (High Speed)
Medipix3 (SPM) (2)	2.5	825	81.7	400	80	1.37 keV @ 10 keV, 300 um Si	7.5
Medipix3 (CSM) (3)	0.5	165	17.2	2020	174	2.03 keV @ 10 keV, 300 um Si	9.3
Timepix3 (4)	$1.3 \cdot 10^{-3}$	0.43	0.43	76 10^5	62	4.07 keV @ 59.5 keV, 300 um Si	15.2
Pixirad Pixie II (5)	0.5	160	17.93	2000	50	1.73 keV @ 60 keV, CdTe	12.5
Samsung PC (6)	NS	NS	NS	NS	68	NS	4.6
Pixirad Pixie III (7)	1	260	28.88	1000	50 (SPM) 100 (CSM)	2 keV @ 20 keV, CdTe	34
Eiger (8)	4.2	750	82.88	238.1	121/160/185	NS	8.8
PXD23K (AGH) (9)	8.55	1520	168.66	117	90	NS	25
IBEX (Dectris) (Instant retrigger) (10)	30	5300	197.33	100	90	850 eV FWHM @ 8 keV (300 um Si)	8
IBEX (Dectris) (paralyzable) (11)	10	1800	186.67	100	90	850 eV FWHM @ 8 keV (300 um Si)	8
UFXC32K (12)	11.8	2100	220	85.03	123	NS	26
LNPIX (13)	NS	NS	NS	NS	60	NS	37
X-Counter PC (14)	1.2	120	13.32	833.33	NS	10 keV @ 60 keV, CdTe	NS
PXD18K (AGH) (15)	5.8	580	64.38	172.41	168	NS	23
FPDR90 (AGH) (16)	8.55	855	94.87	117	91	NS	42
AGH_Fermilab (17)	NS	NS	NS	NS	84 (SPM) 168 (CSM)	NS	34
PXF40 (18)	115	11600	1276.5	8.7	185	NS	105
Tsinghua PC (19)	5	500	52.5	200	< 100	NS	40
Medipix3 (SPM) (20)	4.55	375	21.8	220	80	1.43 keV @ 10 keV, Si	30
Medipix3 (CSM) (21)	0.34	28	4.31	2940	174	4.4 keV @ 60 keV, 2mm CdTe	37.2
XPAD3 (22)	2	118	12.43	500	127	2.3 keV @ 59.5 keV CdTe	40
HEPS-BPIX (23)	5	220	24.67	200	115	NS	36.6
Pilatus 2 (24)	6	203	22.51	166.67	123	1 keV @ 8 keV	20.2
Pilatus 3 (instant retrigger) (25)	15	507	30.02	125	123	1 keV @ 8 keV	20.2
Pilatus 3 (paralyzable) (26)	8	270	28.39	125	123	1 keV @ 8 keV	20.2
Telesystems (27)	0.8	20	2.22	1250	NS	4.88 keV @ 122 keV	94.4
Dosepix (28)	1.64	34	3.76	610	150	3.12 keV @ 35 keV	14.6
Actina (CEA Siemens) (29)	40	790	87.7	25	NS	NS	NS
Hexitec (30)	0.001	0.02	1.8 10^{-3}	1 10^6	NS	0.8 keV @ 60 keV	220
MC1 (Siemens) (31)	NS	NS	44.4	40	NS	5 keV FWHM @ 60 keV	< 125
D2R1 (32)	$40 \cdot 10^{-6}$	$0.44 \cdot 10^{-3}$	0.00	25 10^6	30	584 eV FWHM @ 60 keV	315
ERICA (33)	1	9.2	1.02	1000	90	NS	150
CIX 0.2 (34)	12	96	10.08	83.33	330	NS	3200
Philips ChromAIX1 (35)	38	422	44.33	26.32	400	4.7 keV @ 60 keV	3000
Ajat-0.35 (PC) (36)	2.2	18	1.89	454.55	NS	4 keV @ 122 keV, CdTe	390.6
Ajat-0.35 (ADC) (37)	$4.88 \cdot 10^{-5}$	$4 \cdot 10^{-4}$	0.00	20.5 10^6	NS	4 keV @ 122keV, CdTe	390.6
DxRay-Interon (38)	13.25	53	5.57	75.47	NS	7 keV @ 60 keV, CdTe	NS
Ajat-0.5 (39)	NS	NS	NS	NS	NS	4.7 keV @ 122 keV, CdTe	413.2
Philips ChromAIX2 (40)	42	168	17.64	23.81	260	4.8 keV FWHM @ 60 keV	NS
CEA-MultiX (41)	23	36	3.77	43.48	NS	8.5 keV @ 122 keV, CdTe	10000

a consequence, cannot be bump-bonded to a 2-D sensor. In these chips the size of the sensor pixel does not necessarily match the size of the readout channel. The connection between sensor and readout ASIC is usually done through interposers or through PCB traces as it will be described in Section V.

The measured parameters for the chips connected to sensors are shown in Tables IV and VI. The *maximum count-rates* correspond to the input flux at which the output count-rate saturates which corresponds, for the particular case of the paralyzable model, to the inverse of the dead time [60]. Beyond

TABLE V
PHOTON COUNTING ASICS NOT HYBRIDIZED TO THE SENSOR

Name	Channels	Sensor pixel (μm^2)	Energy thresholds	Peaking time (ns)	Tech. node	Specific information	Ref.
Mythen II (42)	128	50 x 300	1	NS	250 nm	Si strip readout chip, edge-on orientation, designed with radiation hard techniques	[107]
Microdose Mammography (43)	NS	50 x 500	2	NS	NS	Si strip readout chip, edge-on orientation	[108][109]
Redlen module 330 (44)	864	330 x 330	6	NS	NS	Module can be tiled seamlessly on 4 sides. Sensor connected to readout chip through interposer. The module contains 2 chips (i.e. 1728 pixels)	[110]
IDEAS (45)	64	2000 x 400	6	50	NS	Optimized for Cd(Zn)Te linear sensor array	[111][112]
KTH_Lin_SPD (46)	160	500 x 400	8	10-20-40-60	180 nm	Optimized for readout of 16-segment Si-strips oriented edge-on	[33][61][34]
Redlen module 500 (47)	864	500 x 500	6	NS	NS	Module can be tiled seamlessly on 4 sides. Sensor connected to readout chip through interposer. The module contains 2 chips (i.e. 1728 pixels)	[110]
Hamamatsu (48)	64	800 x 500	5	NS	NS	Optimized for Cd(Zn)Te linear sensor array	[113]
BNL (49)	64	2200 x 700	5	40-80-160-320	250 nm	Optimized for CdZnTe sensors, 9th order shaper	[114]
GE-DxRay (50)	128	1000 x 1000	2	30	250 nm	Connected to 2-D CdZnTe by means of interposer board, Clinical images taken with the GE lightSpeed VCT scanner	[103][17]

this value it is no longer possible to linearize the count-rate, resulting in ambiguous and therefore inconsistent datasets. The maximum count-rate columns are expressed in Million counts per second per pixel (Mcps/pixel) and in Million counts per second per millimeter square (Mcps/mm^2). Some ASICs have implemented circuit mechanisms to avoid the nonmonotonic behavior of the curve for the measured versus the incoming flux which is characteristic of the paralyzable model [34], [61], [64], [65]. In these systems, the measured flux per channel tends asymptotically to a value that corresponds to the inverse of the dead time. The maximum count rate that is included in the table for these ASICs corresponds to the input count-rate for which the measured count rate reaches $\sim$95% of its maximum.

The value at which the output count rate deviates by 10% with respect to the input count-rate is also included in the table. When a pixel works at this rate, the impact of pile up in the measured spectrum is not significant ([66], [67]). At this count-rate and for a given dead time value (t), the paralyzable and nonparalyzable models provide an error in the measured input count-rate of less than 6%. However, the *10% count rate deviation* parameter fails to account for the circuit solutions that have been proposed by different groups to linearize the count-rate at high photon fluxes [65], [68].

The channel *dead time* is also included. When measurements are not available for this parameter, the value is extracted from calculations using the applicable count-rate model for that particular chip. In the case of a paralyzable counter model

$$\tau_p = \frac{0.1}{0.9\ (\text{input count rate@10\% loss})}. \tag{6}$$

In the case of a nonparalyzable counter model

$$\tau_{np} = \frac{\ln(1/0.9)}{(\text{input count rate@10\% loss})}. \tag{7}$$

The *electronics noise* or equivalent noise charge (ENC) and the energy resolution are also reported. The ENC is the ratio of the value of the r.m.s. noise to the output amplitude of the pulse due to one single electron at the input of the channel. In other words, the ENC is equal to the detector signal that produces an SNR of 1 at the channel output. Note that the ENC corresponds to an electrical parameter related to a single detection channel whereas the *energy resolution* is usually specified for the full detector system and depends on the detection material being used. Therefore, the energy resolution parameter includes the impact of pixel-to-pixel threshold and gain mismatch.

Please note as well that the values reported on the tables for the maximum count-rates and the energy resolution have a strong dependency on the measurement conditions. For example, the maximum count-rate depends strongly on the incoming beam energy because the energy of the incoming photons determine the amplitude of the pulses in the readout electronics. The threshold energy level programmed on the ASIC has also a large impact on the duration of the pulses that are fed into the counter. This affects significantly the count-rate [69]. Since the measurements presented in the tables were not done under the same measurement conditions, those numbers should not be taken as absolute values to compare the different designs but should be rather used to identify trends and performance envelopes.

V. DETECTOR ARCHITECTURES

Different architectures have been used at system level for the readout of the signal generated in semiconductor detector materials.

A. Hybrid Pixel Detectors

Hybrid pixel detectors consist of a 2-D matrix of microscopic radiation sensitive elements each of which is connected to its own pulse processing electronics. The sensor and the readout electronics are connected using fine pitch flip chip technology (see Fig. 5). One of the main advantages of hybrid pixel detectors is the close integration between the semiconductor detector volume and the readout electronics. This allows to minimize the interconnection parasitic capacitance and inductances obtaining the best possible performance, in terms of low noise and high bandwidth, for a given power consumption. The hybrid pixel detector technology with fine pitch integration is required to achieve pixels with a pitch $< 350\ \mu$m. The CLICPix [115] and the Monch [7] hybrid

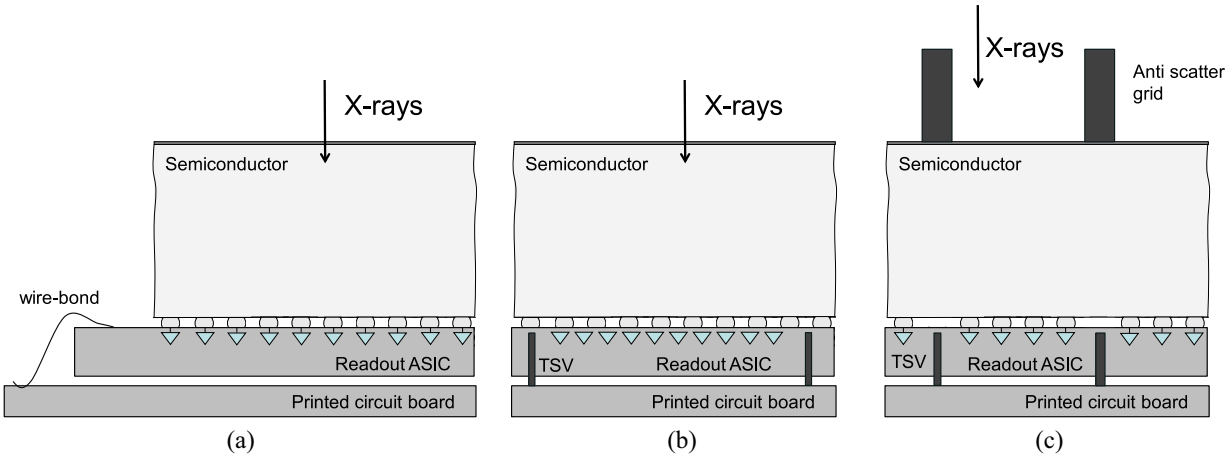

Fig. 5. Schematic drawing of different hybrid pixel detector architectures with respect to the layout of the sensitive area and their interconnections to the PCB. (Plots not to scale.) (a) Typical configuration which has insensitive area required for wire bonding. (b) 4 side buttable fully sensitive area. (c) 4 side buttable, insensitive area underneath anti-scatter grid.

TABLE VI
ELECTRICAL PARAMETERS FOR PHOTON COUNTING ASICS NOT HYBRIDIZED TO THE SENSOR

Name	Max count rate (Mcps/pixel)	Max count rate (Mcps/mm^2)	10% count rate deviation (Mcps/mm^2)	Dead time (ns)	Electronics noise (e^- r.m.s.)	Energy resolution (FWHM)	Power/ channel (μW)
Mythen II (42)	5.88	392	41.18	170	151 + 55.6 e^-/pF	NS	368.75
Microdose Mammography (43)	5.29	212	22.22	189	200 (without detector)	NS	NS
Redlen module 330 (44)	>50	> 500	120	12		~7 keV FWHM @ 60 keV, CZT	<2
IDEAS (45)	4	5	0.53	250	105 + 40 e^-/pF	7 keV @ 60 keV, CdTe (10 pF Cin total)	4200
KTH_Lin_SPD (46)	272	1360	142.8	3.68	214 @ 5pF Cin (40 ns pk time)	1.09 keV @ 15 keV	80000
Redlen module 500 (47)	> 50	> 200	40	12	NS	~8 keV FWHM @ 60 keV, CZT	<2
Hamamatsu (48)	5.5	14	1.44	181.82	NS	12 keV @ 120 keV, CdTe	NS
BNL (49)	4	6	0.58	250	170 @ 2 pF Cin (40ns pk time)	5.5 keV @ 40 ns pk time / 2.15keV @ 320 ns pk time (4.6pF Cin)	4700
GE-DxRay (50)	11.6	12	1.22	86.21	NS	5.8keV @ 122keV, CdZnTe (5pF Cin total)	2100

pixel detectors have achieved a 25 μm pixel pitch although neither chip is aimed at spectroscopic X-ray imaging. A drawback of the technology is the high cost of the interconnection process for relatively low volumes. Fig. 5 illustrates the cross section of hybrid pixel detectors. Fig. 5(a) shows the most typical configuration in which the sensor is connected to the sensitive part of the ASIC, where the pixels are physically laid out. During the readout phase, the data from the pixels is shifted to the periphery of the chip where it is conditioned to be sent off chip through output links. The connection to the PCB is usually done through wire bonding.

The Medipix3 ASIC was used as a test vehicle to explore the interconnection of the readout ASIC to the PCB using through silicon via (TSV) technology. This was a first step toward designing a readout chip that can be tiled seamlessly on four sides [116]. The chip was designed to be "TSV ready," i.e., the design of the wire bonding pads is such that they can be accessed from the back of the chip for TSV processing. TSV's on the IO pads obviate the need for wire bonds further diminishing the required dead area between chips on a large surface [117].

The Medipix4 and Timepix4 chips will implement the functions normally associated with the chip periphery throughout the pixel matrix taking full advantage of the opportunities provided by the TSV process. As the readout logic is no longer confined to one chip edge there is more flexibility in the choice of readout architectures. The chips should be but table on 4 sides. This, however, imposes a design based on slightly smaller ASIC pixel dimensions with respect to the sensor pixels [117].

Göderer and Kreisler [37] have presented the MC1 chip, a four side buttable semiconductor detector readout chip adapted to the CT application using TSV technology. In the presented solution, the functions associated to the chip periphery and the TSV pads are physically located at the space underneath the position of the anti-scatter grid. This is illustrated in Fig. 5(c).

B. Connection Sensor-ASIC With Interposer

Another solution that has been adopted by systems with pixels in the order of 350–500 μm consists of connecting the sensor to the ASIC through an interposer. The interposer is an electrical interface that routes the signals from the sensor to the input of the readout ASIC. The pitch of the sensor pixels does not necessarily match the pitch of the channels in

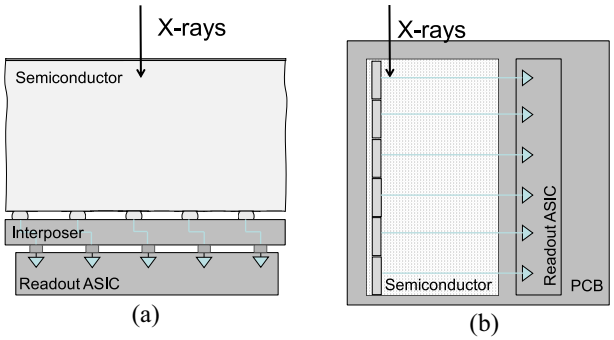

Fig. 6. Drawing of a system connecting the sensor material to the readout ASIC by means of an interposer layer (b). (a) Illustration of a detector edge-on detector system. The photons from the X-ray beam can be read out by different electronic channels depending on the interaction depth. In the real system, the length of the strip segments can be chosen to equalize the flux to be processed by each readout channel. (The plots are not to scale.)

the readout chip. An illustration of this type of connection is shown in Fig. 6, left. Examples of systems in CT using this approach are ASIC-based systems in [110] and [118].

C. Edge-on-Strips

The edge-on-strip technique consists on placing silicon strip detectors along the direction of the beam. The cross section of the detector channel is in the order of $\sim$500 $\times$ 500 μm^2. Fig. 6, right, illustrates this principle. The advantage of this configuration is that silicon is very homogeneous, inexpensive and simple to produce in large volumes. It has short collection times of the induced charge and the mobility lifetime product is orders of magnitude higher than other detector materials.

Since the strip detectors can be segmented in the direction of the beam, the photons can be read out by different electronic channels in the processing ASIC depending on the interaction depth. This allows to reduce the effective flux to be processed by readout channels, further reducing pile up. In the real system, the length of the strip segments can be chosen to equalize the flux to be processed by each readout channel [33].

The routing of the signals from the sensor elements to the readout electronics is complex and adds parasitic capacitances to the input of the front-end. This degrades the noise in the readout channels and the speed in the signals in the pixel readout electronics for a given power consumption.

Silicon, due to its lower atomic number, and for the energies of interest in medical X-ray imaging shows a larger fraction of Compton scattered events which impact the energy response of the system.

A feasibility study for the use of silicon edge-on-strip detectors in CT was presented in [31].

VI. Readout Channel Processing

This section covers aspects related to the signal processing in PCDs.

A. Digitization Methods

Various methods have been used for the digitization of the amplified signal from the sensor. The photon counting ASICs used today as detectors in CT modules contain n discriminators to compare the energy-proportional signal at the output of the shaper with the same number (n) of thresholds. The thresholds are usually implemented as global voltage signals that are generated in the peripheral circuitry of the chip and that are distributed to all detection channels. A local on-pixel digital-to-analog converter (DAC) associated to each comparator is used to compensate for the intrinsic channel-to-channel offset mismatch. Threshold comparison with a given number of discriminator circuits working in parallel is the fastest digitization scheme. However, there is a penalty in power consumption and in the circuit area in the pixel because every threshold level requires one comparator, one threshold-adjustment DAC and digital storage latches to program the optimum code for the DAC. The optimum DAC code is found by means of a calibration procedure.

Gustavsson *et al.* [34] designed a readout channel that works as a digital peak detector. After the detection of a hit by the lowest threshold, the preamplifier output signal is sampled every clock cycle during a programmed time (in the order of 40 ns). When the input signal to any comparator exceeds the corresponding threshold, a digital register is set. After the programmed time, a counter associated to the highest detected threshold is incremented and the analog front-end and the digital registers are reset. The observed count-rate becomes nonparalyzable.

In the Timepix3 [72] and the Dosepix [94] chips, the information on the photon energy is measured using the time-over-threshold (ToT) method. Usually, in the ToT architectures the front-end amplifier consists of a CSA followed by a discriminator [119]. The CSA's feedback capacitor integrates the current pulse induced in the electrode producing a pulse with a fast rising edge and an amplitude proportional to the energy. If the amplitude of the pulse is above a certain value ($\sim V_T \sim$ 26 mV, the thermodynamical voltage at room temperature) then the discharge of the capacitor is done at constant current and as a consequence the preamplifier output voltage pulse returns to the baseline with a constant slope (the preamplifier output time waveform looks triangular with a time duration linear with the energy of the incoming photon). During the time the preamplifier output voltage is above the threshold level, the pixel increments a counter at every clock cycle. The Timepix3 chip combines this digitization scheme with a data push architecture: when the preamplifier output voltage returns to the baseline, the recorded counter value, its time stamp (with 1.56 ns resolution) and the pixel coordinates are encapsulated into a data packet which is sent to the periphery of the chip and subsequently to the readout system. Corrections for charge sharing due to diffusion and fluorescence photons inside the sensor material can be applied offline in the readout system by event correlation using pixel hit time-stamps.

ToT digitization has the advantage of processing the signal in the digital domain (for which very deep submicron CMOS

technologies are optimized). The time required for the preamplifier output to return to its baseline is usually much longer than the peaking time and this limits the count-rate of the system. As a consequence, in order to process every photon correctly, the system can only tolerate a relatively low flux. If a data push architecture is combined with this type of digitization scheme, the requirements on the speed of the output link are very demanding. The amount of information that can be sent off chip sets a limit to the incoming flux that can be processed by the chip. For example, in the case of the Timepix3 chip [72], assuming uniform irradiation across the chip, the maximum count-rate is limited by the data that can be transferred by the output link (5.12 Gb/s) to 0.4 Mcps/mm^2 (every event in a pixel generates a packet of 48 bits).

Analog-to-digital (ADC) converters have also been used for the digitization of the analog signal. In this case, a peak-detect-and-hold circuit [120] is added in the signal processing chain. ADCs have been integrated on-pixel or placed outside the ASIC, in the readout board. The Samsung PC [74] implements a modified version of a successive approximation ADC scheme on the pixel. In the case of the Hexitec system [56], the pixel contains a preamplifier, a shaper and a peak-detect-and-hold circuit. The analog value at the output of the peak detector is digitized by an off-chip ADC (14 bits). The off-pixel digitization leads to a decrease in the maximum count rate.

The pixel circuit presented in [105] and [106] incorporates an 8-bit successive approximation ADC providing 256 energy bin spectrum. A novel analog queuing mechanism is implemented in order to derandomise the photon flux prior to the ADC conversion. This relaxes the value of the ADC sampling frequency and minimizes the probability to lose photons [121].

In addition, the pixel in [106] also integrates three mechanisms to reduce the impact on the energy spectrum of: 1) charge induction; 2) charge sharing; and 3) pile-up. The charge induction refers to the transient bipolar current pulse that develops in a pixel electrode due to the movement of charge carriers collected by a neighboring pixel (see Section III). Depending on system parameters like: 1) ratio between sensor thickness and pixel pitch; 2) the electric field in the sensor; or 3) the speed of the input front-end, this type of cross-talk can lead to a low energy tail in the spectrum (see also Section III). The pixel is able to recognize those pulses by their short time duration. In [106], charge sharing correction is done based on communication between a pixel and its four nearest adjacent neighbors, the decision on the charge allocation being done based on the assignation to the pixel whose discriminator signal arrives first.

B. System Count Rate

The maximum count rate for the chips in Tables III and V is shown in Fig. 7.

The gray line is a guide for the eye that corresponds to a count rate of 10/(pixel area (mm^2)). The red dots correspond to hybrid pixel detector systems whereas the blue dots correspond to systems whereby the readout ASIC is connected to the sensor through an interposer or systems in an edge-on configuration. In general, the trend shows that the smaller the pixel pitch, the highest is the photon flux that can be processed in a given area.

A simulation based on basic semiconductor principles was carried out in order to calculate the pixel electrode induced current time-waveform for the case of a 1-mm thick CdTe sensor (at 600 V bias), with 60 keV photons depositing their energy at a depth equal to their mean free path in the material (i.e., 240 μm) [8]. For a given pixel pitch, the time required to integrate a given fraction of the charge was calculated [$t_i = f$(pitch, percentage of integrated charge)]. The percentages of integrated charge chosen where 90%, 95%, and 97.5%. The red dashed curves correspond to the count rate capability of a detector with a dead time equal to twice the integration time required to account for a given percentage of charge (t_i). This calculation assumes a system with a symmetrical response shaper. These lines indicate a physical limit beyond which the system enters in ballistic deficit and, as a consequence the front-end is not able to integrate a fraction of the signal delivered by the sensor. The dependence of the red dashed lines with the pixel pitch is a consequence of the small pixel effect (Section III). The smaller the pixel pitch with respect to the sensor thickness, the shorter is the induced pulse because the high gradient of the weighting potential is concentrated closer to the pixel electrode (see Fig. 3).

In Fig. 7, bottom, the impact of segmentation in the spectrum measured by one pixel is also shown. A simulation with 80 keV photons impinging on a 2-mm CdTe detector biased at -800 V was carried out. The simulated readout channel had a $\sim 100e^-$ r.m.s. noise (pixel to pixel gain mismatch, offset dispersion, and charge trapping in the detector were not included in the simulation).

The results from these simulations show that for the 1-mm pixel pitch the photopeak is well visible. The peaks from the fluorescence photons at $\sim$23 and $\sim$27 keV are very small. As the pixel pitch is reduced to 300 and 500 mm the main photopeak is reduced and the fluorescence and escape peaks increase in size. In the case of a 100-mm pixel, the impact of charge diffusion as a low energy continuous tail can be seen. This low energy tail completely distorts the information contained in the X-ray beam. For this fine pixel pitch, algorithms have to be applied to correct for charge sharing due to diffusion and fluorescence photons (Section VI).

Note that the outlier (46) in Fig. 7 corresponds to the solution implemented for the readout of silicon strips placed edge-on to the beam [33], [34], [61]. As a consequence, for this particular point in the graph, the remarks above related to 1) the induced pulse duration versus the pixel size and 2) the simulated spectra included in the same figure are not applicable. The high count rate that this solution can achieve is due to the multiple parallel electronic readout channels that are associated to a single sensor pixel element.

Systems labeled (35) and (40) correspond to the ChromAIX1 and ChromAIX2, respectively. Label (29) corresponds to the Actina system. These chips were specifically designed for the human CT application using high-Z sensor materials. The three of them are in a region which is a tradeoff between 1) the ability to process large fluxes (which requires small pixels); 2) the measured spectrum fidelity (for which

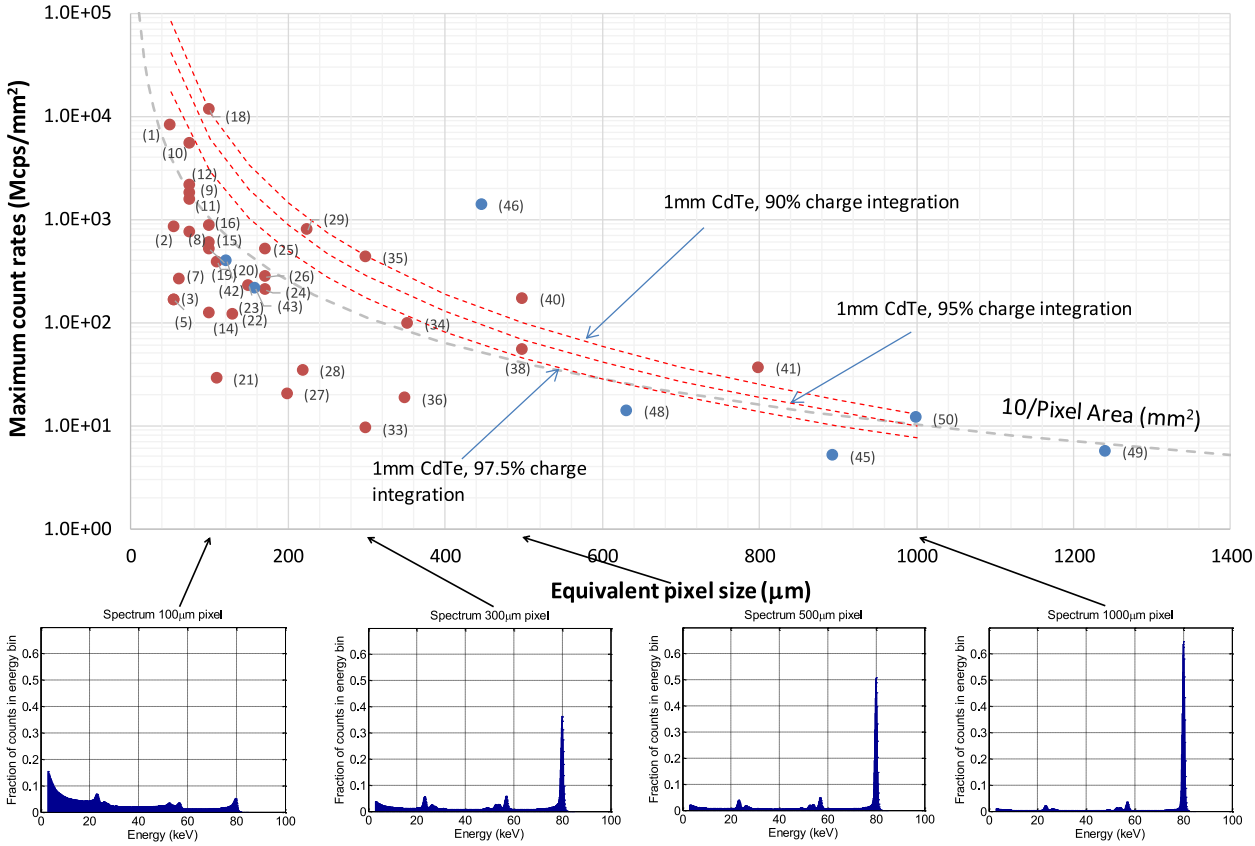

Fig. 7. Maximum count rate as a function of the pixel size. The red marks correspond to hybrid pixel detector readout chips. The blue marks correspond to photon counting ASICs not hybridized to the sensor. The spectra at the bottom correspond to simulations for 80 keV photons impinging on a 2-mm thick CdTe sensor biased at −800 V. The readout channel has an r.m.s. noise of 100e⁻. Charge trapping and gain/offset channel mismatch effects were not included in the simulation.

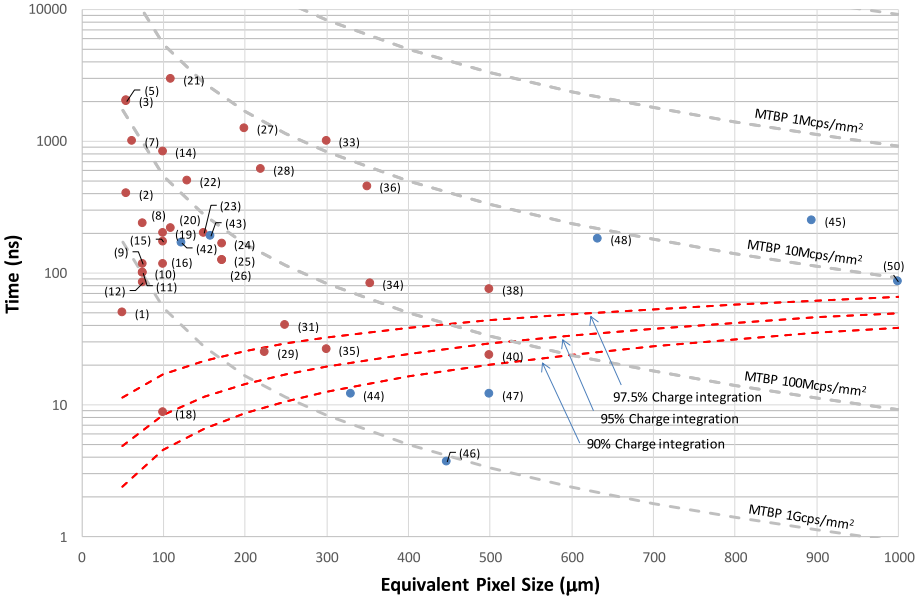

Fig. 8. Dead time as a function of the pixel size. The red marks correspond to hybrid pixel detector readout chips. The blue marks correspond to photon counting ASICs not hybridized to the sensor.

larger pixels are preferred); and 3) the ability to integrate most of the signal delivered by the sensor (the three points are very close to the line indicating the maximum count-rate achievable to integrate 90% of the signal).

Fig. 8 shows the channel dead-time (ns) as a function of the pixel size. The time to integrate a given percentage of the charge (90%, 95%, and 97.5%) is also plotted (red dashed lines). The mean time between consecutive photons (MTBP)

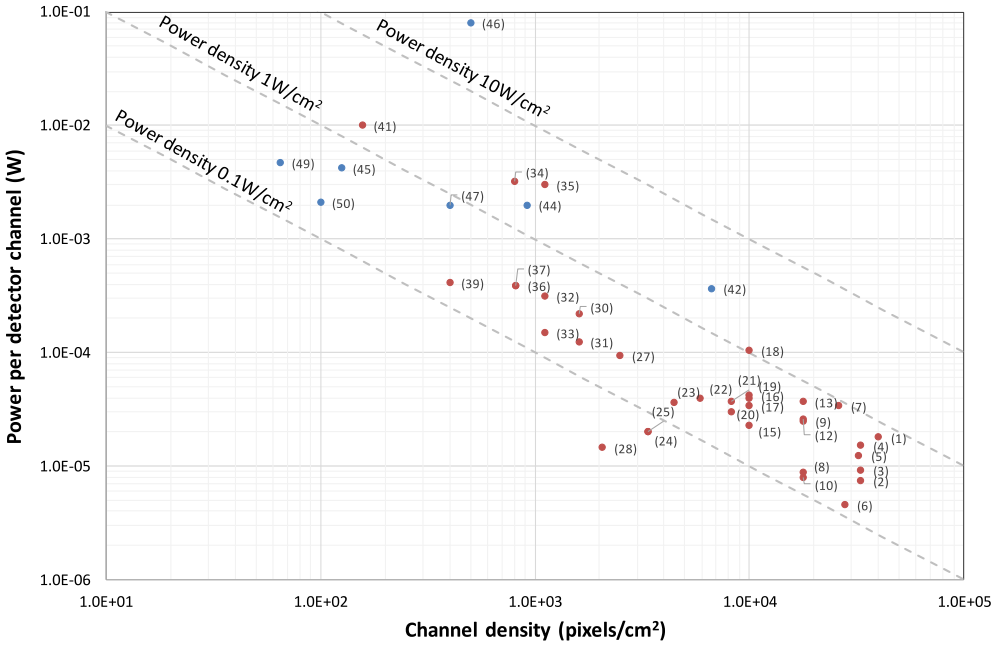

Fig. 9. Power consumption per detector channel as a function of the channel density. The red marks correspond to hybrid pixel detector readout chips. The blue marks correspond to photon counting ASICs not hybridized to the sensor.

are also plotted in gray-dashed, for different values of the incoming flux. Note that the time between consecutive photons follows an exponential distribution.

C. Correction Algorithms

From the on-pixel measurement spectra included in Fig. 7 it can be concluded that the measured energy spectrum is degraded due to charge diffusion and by the effect of the fluorescence photons when the pixel pitch is decreased. The distortion in the energy spectrum increases if the pixel pitch decreases with respect to the sensor thickness.

To retain the energy information of the incoming spectrum at fine pixel pitches, the system must implement an architecture in which the energy deposited by a single incoming photon in a cluster of pixels is reconstructed and the hit is assigned to a single pixel. The algorithm usually assigns the hit to the pixel containing the largest energy deposition.

If the energy of the incoming X-ray photons is larger than twice the sensor material's fluorescence photon energy, more signal will be induced in the location of the initial photon interaction with respect to the location where the fluorescence photon was deposited. For photon energies between the energy of the fluorescence photons and twice this value, the algorithm might produce an error in the assignment because the largest signal is induced at the location where the fluorescence photon deposits its energy.

An algorithm implementing that functionality was integrated in the Medipix3 chip ([122], [123]). This is the so called charge summing mode (CSM). Alternatively, the CSM can be disabled and the pixels operate processing their local charge independently from their neighbors. This is called Single Pixel Mode. Koenig *et al.* [66], [67] studied the properties of the CSM algorithm with respect to the Single Pixel Mode. The charge sharing tail and the peaks from the fluorescence photons are minimized in CSM. The algorithm has also a positive impact in the image reconstruction. A CT scan of a phantom containing different contrast agents shows a 45% gain in contrast for iodine (250 μmol/ml) and 30% gain in contrast for gadolinium [66].

Similar architectures for addressing charge sharing and fluorescence have been implemented in the Pixie III ASIC [75], the X-Counter PC [81], and the AGH_Fermilab chip [84]. The group in AGH is exploring different algorithms for minimization of the charge sharing effects. An overview is presented in [124]. In [97] a fully digital charge sharing correction algorithm is implemented.

D. System Power Consumption

The power consumption of the detector channel is plotted versus the channel density in Fig. 9. Three lines are drawn, corresponding to the power consumption of the channel for a constant density of power consumption (0.1 W/cm^2, 1 W/cm^2, and 10 W/cm^2). The lowest level, 0.1 W/cm^2 corresponds roughly to the limit of heat flux that can be removed by natural air convection with 10 °C temperature rise [125]. Roughly, above 1 W/cm^2 active cooling has to be implemented.

The outlier with label (46) in the plot refers to citation [61] (readout of silicon strips placed edge-on to the beam). An effective sensor channel is read out by 16 parallel readout channels and this, combined with the relatively high input capacitance related to the interconnection between the chip and the readout channel, has an impact in the power consumption density.

The detector temperature usually has to be controlled to avoid changes in the sensor leakage current that could have

an impact on the noise. This is of particular importance with high-Z materials where leakage currents may be particularly high in the presence of crystal defects [126]. Temperature induced leakage currents could also induce front-end saturation if the leakage current compensation circuit cannot cope. Temperature control is also beneficial to avoid (inhomogeneous) temperature induced threshold/gain variations in the readout channels which, in the field of CT, could lead to ring artifacts.

VII. Conclusion

In the past decade there has been a lot of progress to bring direct-conversion pulse-processing detector systems to clinical CT. The direct-conversion technology allows the generation of a large (compared to the traditional indirect systems) and reproducible electronic signal when a photon deposits its energy in the semiconductor sensor material. The photon counting technique consists on processing the electronic signal deposited by the photon on an event-by-event basis in order to classify it in its corresponding energy bin.

Photon counting-based CT systems have demonstrated advantages in comparison to those using energy integrating detection. These benefits are intrinsic to the pulse processing modality and include the simultaneous acquisition of multiple energy bins and the low electronics noise. In addition, their spatial resolution is higher. These benefits lead to improvements in the image quality and/or the reduction in the dose to the patients and enable potential clinical applications. For example: 1) the high spatial resolution and low noise have applications in lung and cardiovascular imaging (stent imaging) and 2) the ability to sample different energy bins can improve material identification by the energy dependence of attenuation and reduce the impact metal artifacts in the image [127].

One of the key elements in the photon counting CT system is the detector and the progress in this element of the chain has been possible thanks to technological advances in sensor manufacturing, microelectronics and fine pitch interconnection techniques.

This article has been written to review the different PCD architectures available and covers the principles from the mechanisms of X-ray energy deposition in the sensor material up to the processing of the electronics signal.

The principles of the interaction of X-ray photons with semiconductor detectors, and the process of signal induction in the input electrodes are discussed. In high-Z detectors, like GaAs, CdTe or CdZnTe, the mobility-lifetime product of electrons is higher than for holes. Therefore, in order to minimize the impact of hole trapping, which leads to a reduction of signal in the collection electrodes, it is of high importance to minimize the hole contribution in the induced signal. This can be done by: 1) biasing the sensor for electron collection and 2) by minimizing the pixel size with respect to the sensor thickness to benefit from the small pixel effect. The small pixel effect has the additional advantage of decreasing the time duration of the induced pulse: 1) minimizing the signal loss due to ballistic deficit and 2) making the system able to process larger photon fluxes.

However, simulations and measurements have shown that fine pixel pitches suffer from distortion in the energy spectrum due to charge sharing and fluorescence photons. This effect has been addressed with architectures in which adjacent pixels communicate in order to reconstruct the total charge deposited by a single photon in an area of the sensor and assign it to a single pixel element.

In addition to the traditional materials typically used as radiation detectors, the authors also included leaded halide perovskites which are gaining some attention in the detector development community for their strong stopping power and their potential low cost.

Hybrid pixel detector readout ASICs were reviewed and it was shown that these detectors, in general, optimize the efficiency of the power consumption per channel for a given count rate and a number of energy bins because the intimate connection between the sensor and the readout electronics reduces parasitic interconnection capacitances at the input of the analog processing chain.

In the geometry with silicon strip sensors oriented "edge-on," the photons deposited at different depths in the sensor are sampled by parallel-working electronic readout channels. This architecture has been shown effective for dealing with high fluxes, but at the expense of increased power density and system complexity.

Continuous advances in sensor materials, microelectronics, and interconnection techniques are making feasible to extract the maximum information contained in the X-ray beam arriving at a given pixel element, i.e., the number of photons in a given time interval, their energies (and their individual times of arrival). These advances will dramatically change the clinical use of CT and other medical imaging modalities in the coming decades.

Acknowledgment

This article has been possible thanks to the contributions of many people. The authors would like to thank: P. Otfinowski and R. Kleczek (AGH), E. Gros d'Aillon and L. Verger (CEA), S. Procz (FMF), B. Yanoff (GE), D. Darambara (The Institute of Cancer Research & the Royal Marsden NHS Foundation), G. Shelkov (JINR), K. Taguchi (Johns Hopkins University), M. Danielsson (KTH, Prismatic Sensors), R. Steadman (Philips), K. Iniewski (Redlen), E. Göderer (Siemens Healthineers), Z. Deng, X. Wang, W. Liu and Y. Liu (Tsinghua University), A. Butler (U. Canterbury, MBI). The authors would also like to acknowledge the members of the Medipix 2, 3, and 4 Collaborations.

References

[1] K. Taguchi and J. S. Iwanczyk, "Vision 20/20: Single photon counting X-ray detectors in medical imaging," *Med. Phys.*, vol. 40, no. 10, 2013, Art. no. 100901, doi: 10.1118/1.4820371.

[2] B. Mikulec, "Single photon detection with semiconductor pixel arrays for medical imaging applications," Ph.D. dissertation, Institut für Isotopenforschung und Kernphysik der, Univ. Vienna, Vienna, Austria, 2000.

[3] B. Dierickx, Q. Yao, N. Witvrouwen, D. Uwaerts, S. Vandewiele, and P. Gao, "X-ray photon counting and two-color X-ray imaging using indirect detection," *Sensors*, vol. 16, no. 6, p. 764, 2016, doi: 10.3390/s16060764.

[4] B. Dierickx, B. Dupont, A. Defernez, and N. Ahmed, "Indirect X-ray photon-counting image sensor with 27T pixel and 15 e^- R.M.S. accurate threshold," in *Dig. Tech. IEEE Int. Solid-State Circuits Conf.*, Jun. 2011, pp. 114–115, doi: 10.1109/ISSCC.2011.5746243.

[5] U. W. Schiebel *et al.*, "Fluoroscopic X-ray imaging with amorphous silicon thin-film arrays," in *Proc. SPIE*, 1994, p. 2163, doi: 10.1117/12.174248.

[6] R. Figueras, J. Sabadell, L. Terés, and F. Serra-Graells, "A 70-μm pitch 8-W self-biased charge-integration active pixel for digital mammography," *IEEE Trans. Biomed. Circuits Syst.*, vol. 5, no. 5, pp. 481–489, Oct. 2011, doi: 10.1109/TBCAS.2011.2151192.

[7] R. Dinapoli *et al.*, "MÖNCH, a small pitch, integrating hybrid pixel detector for X-ray applications," *J. Instrum.*, vol. 9, no. 5, May 2014, Art. no. C05015, doi: 10.1088/1748-0221/9/05/C05015.

[8] R. Ballabriga *et al.*, "Review of hybrid pixel detector readout ASICs for spectroscopic X-ray imaging," *J. Instrum.*, vol. 11, no. 1, 2016, Art. no. P01007, doi: 10.1088/1748-0221/11/01/P01007.

[9] T. G. Schmidt, "Optimal 'image-based' weighting for energy-resolved CT," *Med. Phys.*, vol. 36, no. 7, pp. 3018–3027, 2009, doi: 10.1118/1.3148535.

[10] H. Hull *et al.*, "iDXA, prodigy, and DPXL dual-energy X-ray absorptiometry whole-body scans: A cross-calibration study," *J. Clin. Densitometry*, vol. 12, no. 1, pp. 95–102, 2009, doi: 10.1016/j.jocd.2008.09.004.

[11] M. Lundqvist, M. Danielsson, B. Cederstroem, V. Chmill, A. Chuntonov, and M. Aslund, "Measurements on a full-field digital mammography system with a photon counting crystalline silicon detector," *Phys. Med. Imag.*, vol. 5030, p. 547, Dec. 2014, doi: 10.1117/12.480251.
[Online]. Available: https://www.spiedigitallibrary.org/conference-proceedings-of-spie/5030/1/Measurements-on-a-full-field-digital-mammography-system-with-a/10.1117/12.480251.short?SSO=1

[12] M. J. Willemink, M. Persson, A. Pourmorteza, N. J. Pelc, and D. Fleischmann, "Photon-counting CT: Technical principles and clinical prospects," *Radiology*, vol. 289, no. 2, pp. 293–312, 2018, doi: 10.1148/radiol.2018172656.

[13] J. S. Iwanczyk *et al.*, "Photon counting energy dispersive detector arrays for X-ray imaging," *IEEE Nucl. Sci. Symp. Conf. Rec.*, vol. 4, Jan. 2007, pp. 2741–2748, doi: 10.1109/NSSMIC.2007.4436710.

[14] A. Z. O. Benjaminov, E. Perlow, Z. Romman, R. Levinson, B. Bashara, and M. Cohen, "Novel, energy-discriminating photon counting CT system (EDCT): First clinical evaluation—CT angiography: Carotid artery stenosis," in *Proc. Radiol. Soc. North Amer. Sci. Assemble Annu. Meeting*, 2008, pp. 15–17.

[15] R. L. Z. Romman, O. Benjaminov, and E. Perlow, "Photon counting CT system (EDCT) versus nominal MSCT: Comparison of stenosis measurement using step wedge teflon-iodine phantom," in *Proc. Radiol. Soc. North Amer. Sci. Assemble Annu. Meeting*, 2008, Art. no. 7002522.

[16] I. S. Z. Romman *et al.*, "Virtual noncontrast CT of the abdomen using a dual energy photon-counting CT scanner: Assessment of performance," in *Proc. Radiol. Soc. North Amer. Sci. Assemble Annu. Meeting*, 2009, Art. no. 8012798.

[17] D. Moraes, E. Nygard, and A. Rudge, "Front-end electronics for the readout of CdZnTe sensors," in *Proc. IEEE Nucl. Sci. Symp. Conf. Rec.*, vol. 1, 2005, pp. 348–352, doi: 10.1109/NSSMIC.2005.1596268.

[18] G. Pelc and P. Edic. (2018). *High Dose Efficiency CT System*. [Online]. Available: https://projectreporter.nih.gov/project_info_description.cfm?aid=9388345&icde=40662306

[19] R. K. Panta *et al.*, "Element-specific spectral imaging of multiple contrast agents: A phantom study," *J. Instrum.*, vol. 13, no. 2, pp. 2126–2134, 2018, doi: 10.1088/1748-0221/13/02/T02001.

[20] F. Ostadhossein *et al.*, "Multi-'color' delineation of bone microdamages using ligand-directed sub-5 nm Hafnia nanodots and photon counting CT imaging," *Adv. Funct. Mater.*, vol. 30, no. 4, Jan. 2020, Art. no. 1904936.

[21] P. H. Butler *et al.*, "MARS pre-clinical imaging: The benefits of small pixels and good energy data," in *Proc. SPIE Dev. X-Ray Tomography XII*, 2019, Art. no. 111130C.

[22] L. K. Stamp *et al.*, "Clinical utility of multi-energy spectral photon-counting computed tomography in crystal arthritis," *Arthritis Rheumatol.*, vol. 71, no. 7, pp. 1158–1162, 2019.

[23] R. K. Panta *et al.*, "First human imaging with MARS photon-counting CT," in *Proc. IEEE Nucl. Sci. Symp. Med. Imag. Conf. (NSS/MIC)*, 2018, pp. 1–7, doi: 10.1109/NSSMIC.2018.8824513.

[24] M. F. Walsh *et al.*, "First CT using Medipix3 and the MARS-CT-3 spectral scanner," *J. Instrum.*, vol. 6, no. 1, 2011, Art. no. C01095, doi: 10.1088/1748-0221/6/01/C01095.

[25] S. Feuerlein *et al.*, "Multienergy photon-counting K-edge imaging: Potential for improved luminal depiction in vascular imaging," *Radiology*, vol. 249, no. 3, pp. 1010–1016, 2008.

[26] E. Roessl *et al.*, "Imaging performance of a photon-counting computed tomography prototype," in *Proc. 3rd Workshop Med. Appl. Spectroscope X-Ray Detect.*, 2015, p. 3.

[27] D. Muenzel, M. Bartels, F. K. Kopp, B. Brendel, R. Proksa, and P. Douek, "Spectral photon-counting CT? Initial experience with dual—Contrast agent K-edge colonography," *Radiology*, vol. 283, no. 3, pp. 723–728, 2017.

[28] F. K. Kopp *et al.*, "Evaluation of a preclinical photon-counting CT prototype for pulmonary imaging," *Sci. Rep.*, vol. 8, no. 1, pp. 1–9, 2018, doi: 10.1038/s41598-018-35888-1.

[29] C. Herrmann, R. Steadman, and O. Mulhens, "ChromAIX: Fast energy resolved photon-counting readout electronics for future human computed tomography," in *Proc. IEEE Nucl. Sci. Symp. Conf. Rec.*, 2010, pp. 1996–1999, doi: 10.1109/NSSMIC.2010.5874125.

[30] R. Steadman, C. Herrmann, and A. Livne, "ChromAIX2: A large area, high count-rate energy-resolving photon counting ASIC for a spectral CT prototype," *Nucl. Instrum. Methods Phys. Res. A Accelerators Spectrometers Detectors Assoc. Equip.*, vol. 862, pp. 18–24, Aug. 2017, doi: 10.1016/j.nima.2017.05.010.

[31] H. Bornefalk and M. Danielsson, "Photon-counting spectral computed tomography using silicon strip detectors: A feasibility study," *Phys. Med. Biol.*, vol. 55, no. 7, pp. 1999–2022, 2010, doi: 10.1088/0031-9155/55/7/014.

[32] M. Persson *et al.*, "Energy-resolved CT imaging with a photon-counting silicon-strip detector," *Phys. Med. Biol.*, vol. 59, no. 22, pp. 6709–6727, 2014, doi: 10.1088/1361-6560/59/22/6709.

[33] M. Danielsson, "A silicon strip detector for photon counting spectral computed tomography," in *Proc. 3rd Workshop Med. Appl. Spectroscope X-Ray Detect.*, 2015, p. 10.

[34] M. Gustavsson, F. U. Amin, A. Björklid, A. Ehliar, C. Xu, and C. Svensson, "A high-rate energy-resolving photon-counting ASIC for spectral computed tomography," *IEEE Trans. Nucl. Sci.*, vol. 59, no. 1, pp. 30–39, Feb. 2012, doi: 10.1109/TNS.2011.2169811.

[35] Z. Yu *et al.*, "Evaluation of conventional imaging performance in a research whole-body CT system with a photon-counting detector array," *Phys. Med. Biol.*, vol. 61, no. 4, pp. 1572–1595, 2016, doi: 10.1088/0031-9155/61/4/1572.

[36] E. Kraft, F. Glasser, S. Janssen, S. Kappler, D. Niederloehner, and P. Villard, "ASIC design for photon counting computed tomography," in *Proc. 1st Workshop Med. Appl. Spectroscope X-Ray Detect.*, 2011, p. 10.

[37] E. Göderer and B. Kreisler, "A four-side-buttable photon counting ASIC for computed tomography," in *Proc. 5th Workshop Med. Appl. Spectroscope X-Ray Detect. Geneva*, 2019, pp. 7–28.

[38] A. Pourmorteza *et al.*, "Photon-counting CT of the brain: *In vivo* human results and image-quality assessment," *Amer. J. Neuroradiol.*, vol. 38, no. 12, pp. 2257–2263, 2017, doi: 10.3174/ajnr.A5402.

[39] R. Symons *et al.*, "Feasibility of dose-reduced chest CT with photon-counting detectors: Initial results in humans," *Radiology*, vol. 285, no. 3, pp. 980–989, 2017, doi: 10.1148/radiol.2017162587.

[40] S. Si-Mohamed *et al.*, "Review of an initial experience with an experimental spectral photon-counting computed tomography system," *Nucl. Instrum. Methods Phys. Res. A Accelerators Spectrometers Detectors Assoc. Equip.*, vol. 873, pp. 27–35, Nov. 2017, doi: 10.1016/j.nima.2017.04.014.

[41] K. Rajendran *et al.*, "Reducing beam hardening effects and metal artefacts in spectral CT using Medipix3RX," *J. Instrum.*, vol. 9, no. 3, 2014, Art. no. P03015, doi: 10.1088/1748-0221/9/03/P03015.

[42] S. Si-Mohamed *et al.*, "Multicolour imaging with spectral photon-counting CT: A phantom study," *Eur. Radiol. Exp.*, vol. 2, no. 1, p. 34, 2018, doi: 10.1186/s41747-018-0063-4.

[43] S. Si-Mohamed *et al.*, "Evaluation of spectral photon counting computed tomography K-edge imaging for determination of gold nanoparticle biodistribution *in vivo*," *Nanoscale*, vol. 9, no. 46, pp. 18246–18257, 2017, doi: 10.1039/C7NR01153A.

[44] D. Muenzel *et al.*, "Simultaneous dual-contrast multi-phase liver imaging using spectral photon-counting computed tomography: A proof-of-concept study," *Eur. Radiol. Exp.*, vol. 1, no. 1, pp. 1–9, 2017, doi: 10.1186/s41747-017-0030-5.

[45] D. P. Cormode *et al.*, "Multicolor spectral photon-counting computed tomography: *In vivo* dual contrast imaging with a high count rate scanner," *Sci. Rep.*, vol. 7, no. 1, pp. 1–11, 2017, doi: 10.1038/s41598-017-04659-9.

[46] P. Födisch, M. Berthel, B. Lange, T. Kirschke, W. Enghardt, and P. Kaever, "Charge-sensitive front-end electronics with operational amplifiers for CdZnTe detectors," *J. Instrum.*, vol. 11, no. 9, pp. 2104–2109, 2016, doi: 10.1088/1748-0221/11/09/T09001.

[47] S. Ramo, "Currents induced by electron motion," *Proc. IRE*, vol. 27, p. 584, Sep. 1939.

[48] S. del Sordo, L. Abbene, E. Caroli, A. M. Mancini, A. Zappettini, and P. Ubertini, "Progress in the development of CdTe and CdZnTe semiconductor radiation detectors for astrophysical and medical applications," *Sensors*, vol. 9, no. 5, pp. 3491–3526, 2009, doi: 10.3390/s90503491.

[49] E. Hamann, "Characterization of high resistivity GaAs material for photon counting semiconductor pixel detectors," Ph.D. dissertation, Elect. Eng., Univ. Freiburg, Freiburg im Breisgau, Germany, 2013.

[50] B. Thomas, M. C. Veale, M. D. Wilson, P. Seller, A. Schneider, and K. Iniewski, "Characterisation of Redlen high-flux CdZnTe," *J. Instrum.*, vol. 12, no. 12, pp. 1255–1259, 2017, doi: 10.1088/1748-0221/12/12/C12045.

[51] Y. He *et al.*, "Resolving the energy of X-ray photons with MAPbI3 single crystals," *ACS Photon.*, vol. 5, no. 10, pp. 4132–4138, 2018, doi: 10.1021/acsphotonics.8b00873.

[52] E. Frojdh *et al.*, "Count rate linearity and spectral response of the Medipix3RX chip coupled to a 300silicon sensor under high flux conditions," *J. Instrum.*, vol. 9, no. 4, 2014, Art. no. C04028, doi: 10.1088/1748-0221/9/04/C04028.

[53] D. Pennicard *et al.*, "A germanium hybrid pixel detector with 55," *J. Instrum.*, vol. 9, no. 12, 2014, Art. no. P12003, doi: 10.1088/1748-0221/9/12/P12003.

[54] P. Smolyanskiy *et al.*, "Properties of GaAs:Cr-based Timepix detectors," *J. Instrum.*, vol. 13, no. 2, 2018, Art. no. T02005, doi: 10.1088/1748-0221/13/02/T02005.

[55] D. Kozhevnikov and P. Smolyanskiy, "Stack of timepix-based detectors with Si, GaAs:Cr and CdTe sensors with optimized thickness for spectral CT," *J. Instrum.*, vol. 14, no. 2, 2019, Art. no. C02010, doi: 10.1088/1748-0221/14/02/C02010.

[56] L. Jones, P. Seller, M. Wilson, and A. Hardie, "HEXITEC ASIC-a pixellated readout chip for CZT detectors," *Nucl. Instrum. Methods Phys. Res. A Accelerators Spectrometers Detectors Assoc. Equip.*, vol. 604, nos. 1–2, pp. 34–37, 2009, doi: 10.1016/j.nima.2009.01.046.

[57] S. Yakunin *et al.*, "Detection of X-ray photons by solution-processed lead halide perovskites," *Nat. Photon.*, vol. 9, no. 7, pp. 444–449, 2015, doi: 10.1038/nphoton.2015.82.

[58] E. Gros-D'Aillon *et al.*, "Towards large area photon counting flat panel detectors for medical spectral radiography," *5th Work. Med. Appl. Spectrosc. X-Ray Detect. Cern. Geneva*, 2019, pp. 9–18.

[59] H. Wei and J. Huang, "Halide lead perovskites for ionizing radiation detection," *Nat. Commun.*, vol. 10, no. 1, pp. 1–12, 2019, doi: 10.1038/s41467-019-08981-w.

[60] G. F. Knoll, *Radiation Detection and Measurement*, 4th ed. New York, NY, USA: Wiley, 2010, p. 830.

[61] C. Xu *et al.*, "Evaluation of a second-generation ultra-fast energy-resolved ASIC for photon-counting spectral CT," *IEEE Trans. Nucl. Sci.*, vol. 60, no. 1, pp. 437–445, Feb. 2013, doi: 10.1109/TNS.2012.2228276.

[62] K. Taguchi *et al.*, "Modeling the performance of a photon counting X-ray detector for CT: Energy response and pulse pileup effects," *Med. Phys.*, vol. 38, no. 2, pp. 1089–1102, 2011, doi: 10.1118/1.3539602.

[63] K. Taguchi, E. C. Frey, X. Wang, J. S. Iwanczyk, and W. C. Barber, "An analytical model of the effects of pulse pileup on the energy spectrum recorded by energy resolved photon counting X-ray detectors," *Med. Phys.*, vol. 37, no. 8, pp. 3957–3969, 2010, doi: 10.1118/1.3429056.

[64] M. Bochenek *et al.*, "IBEX: Versatile readout ASIC with spectral imaging capability and high count rate capability," *IEEE Trans. Nucl. Sci.*, vol. 65, no. 6, pp. 1285–1291, Jun. 2018, doi: 10.1109/TNS.2018.2832464.

[65] T. Loeliger, C. Bronnimann, T. Donath, M. Schneebeli, R. Schnyder, and P. Trub, "The new PILATUS3 ASIC with instant retrigger capability," in *Proc. IEEE Nucl. Sci. Symp. Conf. Rec.*, 2012, pp. 610–615, doi: 10.1109/NSSMIC.2012.6551180.

[66] T. Koenig *et al.*, "How spectroscopic X-ray imaging benefits from inter-pixel communication," *Phys. Med. Biol.*, vol. 59, no. 20, pp. 6195–6213, 2014, doi: 10.1088/0031-9155/59/20/6195.

[67] T. Koenig *et al.*, "Charge summing in spectroscopic X-ray detectors with high-Z sensors," *IEEE Trans. Nucl. Sci.*, vol. 60, no. 6, pp. 4713–4718, Dec. 2013, doi: 10.1109/TNS.2013.2286672.

[68] V. Radicci *et al.*, "EIGER a new single photon counting detector for X-ray applications: Performance of the chip," *J. Instrum.*, vol. 7, no. 2, 2012, Art. no. 163176, doi: 10.1088/1748-0221/7/02/C02019.

[69] E. Kraft, F. Glasser, S. Kappler, D. Niederloehner, and P. Villard, "Experimental evaluation of the pile-up trigger method in a revised quantum-counting CT detector," in *Proc. Phys. Med. Imag.*, vol. 8313, 2012, Art. no. 83134A, doi: 10.1117/12.911231.

[70] P. Otfinowski, G. Deptuch, and P. Maj, "FRIC—A 50 pixel-pitch single photon counting ASIC with pattern recognition algorithm in 40 nm CMOS technology," *J. Instrum.*, vol. 15, no. 1, 2020, Art. no. C01016.

[71] R. Ballabriga *et al.*, "The medipix3RX: A high resolution, zero dead-time pixel detector readout chip allowing spectroscopic imaging," *J. Instrum.*, vol. 8, no. 2, 2013, Art. no. C02016, doi: 10.1088/1748-0221/8/02/C02016.

[72] T. Poikela *et al.*, "Timepix3: A 65K channel hybrid pixel readout chip with simultaneous ToA/ToT and sparse readout," *J. Instrum.*, vol. 9, no. 5, 2014, Art. no. C05013, doi: 10.1088/1748-0221/9/05/C05013.

[73] R. Bellazzini, G. Spandre, A. Brez, M. Minuti, M. Pinchera, and P. Mozzo, "Chromatic X-ray imaging with a fine pitch CdTe sensor coupled to a large area photon counting pixel ASIC," *J. Instrum.*, vol. 8, no. 2, p. 8, 2013, doi: 10.1088/1748-0221/8/02/C02028.

[74] H.-S. Kim *et al.*, "An asynchronous sampling-based 128 × 128 direct photon-counting X-ray image detector with multi-energy discrimination and high spatial resolution," *IEEE J. Solid-State Circuits*, vol. 48, no. 2, pp. 541–558, Feb. 2013, doi: 10.1109/JSSC.2012.2221196.

[75] R. Bellazzini *et al.*, "PIXIE III: A very large area photon-counting CMOS pixel ASIC for sharp X-ray spectral imaging," *J. Instrum.*, vol. 10, no. 1, 2015, Art. no. C01032, doi: 10.1088/1748-0221/10/01/C01032.

[76] R. Dinapoli *et al.*, "EIGER: Next generation single photon counting detector for X-ray applications," *Nucl. Instrum. Methods Phys. Res. A Accelerators Spectrometers Detectors Assoc. Equip.*, vol. 650, no. 1, pp. 79–83, 2011, doi: 10.1016/j.nima.2010.12.005.

[77] P. Maj, P. Grybos, P. Kmon, and R. Szczygiel, "23552-channel IC for single photon counting pixel detectors with 75 μm pitch, ENC of 89 e^- rms, 19 e^- rms offset spread and 3% rms gain spread," in *Proc. Eur. Solid-State Circuits Conf.*, 2014, pp. 147–150, doi: 10.1109/ESSCIRC.2014.6942043.

[78] P. Grybos, P. Kmon, P. Maj, and R. Szczygiel, "32k channel readout IC for single photon counting pixel detectors with 75 μm pitch, dead time of 85 ns, 9 e^- rms offset spread and 2% RMS gain spread," *IEEE Trans. Nucl. Sci.*, vol. 63, no. 2, pp. 1155–1161, Apr. 2016, doi: 10.1109/TNS.2016.2523260.

[79] R. Kleczek *et al.*, "SPC pixel IC with 9.4 e^- rms offset spread, 60 e^- rms ENC and 70 kfps frame rate," in *Proc. IEEE 45th Eur. Solid-State Circuits Conf. (ESSCIRC)*, 2019, pp. 85–88, doi: 10.1109/ESSCIRC.2019.8902905.

[80] U. Zscherpel *et al.*, "Digital radiology with photon counting detectors," in *Proc. 11th Eur. Conf. Non destructive Test.*, 2014, pp. 308–310.

[81] N. Weber, C. Ullberg, C. Eriksson, M. Urech, and A. Stewart, "Photon counting dual energy X-ray imaging at CT count rates: Measurements and implications of in-pixel charge sharing correction," in *Proc. SPIE*, 2018, p. 44, doi: 10.1117/12.2293591.

[82] R. Szczygiel, P. Grybos, P. Maj, and M. Zoladz, "PXD18k—Fast single photon counting chip with energy window for hybrid pixel detector," in *Proc. IEEE Nucl. Sci. Symp. Conf. Rec.*, 2011, pp. 932–937, doi: 10.1109/NSSMIC.2011.6154126.

[83] R. Szczygiel, P. Grybos, and P. Maj, "A low noise, fast pixel readout IC working in single photon counting mode with energy window selection in 90 nm CMOS," in *Proc. IEEE Int. Symp. Circuits Syst.*, 2011, pp. 1415–1418, doi: 10.1109/ISCAS.2011.5937838.

[84] P. Grybos, P. Maj, L. Ramello, and K. Swientek, "Measurements of matching and high count rate performance of multichannel ASIC for digital X-ray imaging systems," *IEEE Trans. Nucl. Sci.*, vol. 54, no. 4, pp. 1207–1215, Aug. 2007, doi: 10.1109/TNS.2007.903176.

[85] R. Kleczek, P. Grybos, R. Szczygiel, and P. Maj, "Single photon-counting pixel readout chip operating up to 1.2 Gcps/mm^2 for digital X-ray imaging systems," *IEEE J. Solid-State Circuits*, vol. 53, no. 9, pp. 2651–2662, Sep. 2018, doi: 10.1109/JSSC.2018.2851234.

[86] X. Wang, Z. Deng, W. Liu, and Y. Liu, "Development of a pixel readout ASIC for CZT detectors for spectral X-ray photon-counting imaging applications," *J. Instrum.*, vol. 15, no. 01, 2020, Art. no. C01030.

[87] P. Pangaud *et al.*, "XPAD3: A new photon counting chip for X-ray CT-scanner," *Nucl. Instrum. Methods Phys. Res. A Accelerators Spectrometers Detectors Assoc. Equip.*, vol. 571, nos. 1–2, pp. 321–324, 2007, doi: 10.1016/j.nima.2006.10.092.

[88] P. Pangaud *et al.*, "XPAD3-S: A fast hybrid pixel readout chip for X-ray synchrotron facilities," *Nucl. Instrum. Methods Phys. Res. A Accelerators Spectrometers Detectors Assoc. Equip.*, vol. 591, no. 1, pp. 159–162, 2008, doi: 10.1016/j.nima.2008.03.047.

[89] W. Wei *et al.*, "HEPS-BPIX, a single photon counting pixel detector with a high frame rate for the HEPS project," *Nucl. Instrum. Methods Phys. Res. A Accelerators Spectrometers Detectors Assoc. Equip.*, vol. 835, pp. 169–176, Nov. 2016, doi: 10.1016/j.nima.2016.08.033.

[90] J. Gu *et al.*, "A high frame rate test system for the HEPS-BPIX based on NI-sbRIO board," *IEEE Trans. Nucl. Sci.*, vol. 64, no. 6, pp. 1316–1319, Jun. 2017, doi: 10.1109/TNS.2017.2706274.

[91] P. Kraft, "PILATUS 2M a detector for small angle X-ray scattering," Eidgenössische Technische Hochschule, ETH Zürich, Zürich, Switzerland, 2010, doi: 10.3929/ethz-a-006023165.

[92] P. Kraft *et al.*, "Characterization and calibration of PILATUS detectors," *IEEE Trans. Nucl. Sci.*, vol. 56, no. 3, pp. 758–764, Jun. 2009, doi: 10.1109/TNS.2008.2009448.

[93] K. Ogawa *et al.*, "Development of an energy-binned photon-counting detector for X-ray and gamma-ray imaging," *Nucl. Instrum. Methods Phys. Res. A Accelerators Spectrometers Detectors Assoc. Equip.*, vol. 664, no. 1, pp. 29–37, 2012, doi: 10.1016/j.nima.2011.10.009.

[94] W. S.-W. Wong, "A hybrid pixel detector ASIC with energy binning for real-time, spectroscopic dose measurements," Ph.D. dissertation, Dept. Comput. Sci., Mid-Sweden University, Sundsvall, Sweden, 2012.

[95] S. Kappler, F. Glasser, S. Janssen, E. Kraft, and M. Reinwand, "A research prototype system for quantum-counting clinical CT," in *Proc. Phys. Med. Imag.*, vol. 7622, 2010, Art. no. 76221Z, doi: 10.1117/12.844238.

[96] A. Michalowska, "Studies and development of a readout ASIC for pixelated CdTe detectors for space applications," Ph.D. dissertation, École Doctorale: Sciences et Technologies de l'Information, des Télécommunications et des Systèmes, Université Paris Sud, Orsay, France 2013.

[97] J. G. Macias-Montero *et al.*, "ERICA: An energy resolving photon counting readout ASIC for X-ray in-line cameras," *J. Instrum.*, vol. 11, no. 12, p. 8, 2016, doi: 10.1088/1748-0221/11/12/C12027.

[98] E. Kraft, "Universit at Bonn Physikalisches Institut counting and integrating microelectronics development for," Ph.D. dissertation, Physikalisches Institut, Univ. Bonn, Bonn, Germany, 2008.

[99] E. Kraft *et al.*, "Counting and integrating readout for direct conversion X-ray imaging: Concept, realization and first prototype measurements," *IEEE Trans. Nucl. Sci.*, vol. 54, no. 2, pp. 383–390, Apr. 2007, doi: 10.1109/TNS.2007.891571.

[100] L. J. Meng, J. W. Tan, K. Spartiotis, and T. Schulman, "Preliminary evaluation of a novel energy-resolved photon-counting gamma ray detector," *Nucl. Instrum. Methods Phys. Res. A Accelerators Spectrometers Detectors Assoc. Equip.*, vol. 604, no. 3, pp. 548–554, 2009, doi: 10.1016/j.nima.2009.02.043.

[101] H. M. Cho, H. J. Kim, Y. N. Choi, S. W. Lee, H. J. Ryu, and Y. J. Lee, "The effects of photon flux on energy spectra and imaging characteristics in a photon-counting X-ray detector," *Phys. Med. Biol.*, vol. 58, no. 14, pp. 4865–4879, 2013, doi: 10.1088/0031–9155/58/14/4865.

[102] W. C. Barber *et al.*, "High flux energy-resolved photon-counting X-ray imaging arrays with CdTe and CdZnTe for clinical CT," in *Proc. 3rd Int. Conf. Adv. Nucl. Instrum. Meas. Methods Appl. (ANIMMA)*, 2013, p. 4, doi: 10.1109/ANIMMA.2013.6728030.

[103] W. C. Barber *et al.*, "Photon-counting energy-resolving CdTe detectors for high-flux X-ray imaging," in *Proc. IEEE Nucl. Sci. Symp. Conf. Rec.*, 2010, pp. 3953–3955, doi: 10.1109/NSSMIC.2010.5874556.

[104] K. Spartiotis *et al.*, "A photon counting CdTe gamma- and X-ray camera," *Nucl. Instrum. Methods Phys. Res. A Accelerators Spectrometers Detectors Assoc. Equip.*, vol. 550, nos. 1–2, pp. 267–277, 2005, doi: 10.1016/j.nima.2005.04.081.

[105] L. Verger, "A corrected photon counting detector for CT application," *5th Work. Med. Appl. Spectrosc. X-Ray Detect. Geneva*, 2019, pp. 5–29.

[106] A. Peizerat, J. Rostaing, P. Ouvrier-Buffet, S. Stanchina, P. Radisson, and E. Marché, "A 256 energy bin spectrum X-ray photon-counting image sensor providing 8Mcounts/s/pixel and on-chip charge sharing, charge induction and pile-up corrections," in *Proc. Symp. VLSI Circuits*, 2017, pp. C246–C247.

[107] B. Schmitt *et al.*, "Mythen detector system," *Nucl. Instrum. Methods Phys. Res. A Accelerators Spectrometers Detectors Assoc. Equip.*, vol. 501, no. 1, pp. 267–272, 2003, doi: 10.1016/S0168-9002(02)02045-4.

[108] E. Fredenberg, M. Lundqvist, B. Cederström, M. Åslund, and M. Danielsson, "Energy resolution of a photon-counting silicon strip detector," *Nucl. Instrum. Methods Phys. Res. A Accelerators Spectrometers Detectors Assoc. Equip.*, vol. 613, no. 1, pp. 156–162, 2010, doi: 10.1016/j.nima.2009.10.152.

[109] E. Fredenberg, M. Hemmendorff, B. Cederström, M. Åslund, and M. Danielsson, "Contrast-enhanced spectral mammography with a photon-counting detector," *Med. Phys.*, vol. 37, no. 5, pp. 2017–2029, 2010, doi: 10.1118/1.3371689.

[110] C. Hansson, E. Guliyev, G. Prekas, M. Ayukawa, and K. Iniewski, "Performance characteristics detector module for spectral computed tomography," in *Proc. 5th Workshop Med. Appl. Spectroscopy X-Ray Detect. Geneva*, 2019, pp. 6–27.

[111] S. Mikkelsen, D. Meier, G. Mrehlum, P. Øya, B. Sundal, and J. Talebi, "An ASIC for multi-energy X-ray counting," in *Proc. IEEE Nucl. Sci. Symp. Conf. Rec.*, 2008, pp. 1996–2001, doi: 10.1109/NSSMIC.2008.4774870.

[112] X. Wang, D. Meier, K. Taguchi, D. J. Wagenaar, B. E. Patt, and E. C. Frey, "Material separation in X-ray CT with energy resolved photon-counting detectors," *Med. Phys.*, vol. 38, no. 3, pp. 1534–1546, 2011, doi: 10.1118/1.3553401.

[113] Y. Tomita *et al.*, "X-ray color scanner with multiple energy differentiate capability," in *Proc. IEEE Nucl. Sci. Symp. Conf. Rec.*, vol. 6, 2004, pp. 3733–3737, doi: 10.1109/nssmic.2004.1466692.

[114] G. De Geronimo, A. Dragone, J. Grosholz, P. O'Connor, and E. Vernon, "ASIC with multiple energy discrimination for high-rate photon counting applications," in *Proc. IEEE Nucl. Sci. Symp. Conf. Rec.*, vol. 2, 2006, pp. 697–704, doi: 10.1109/NSSMIC.2006.355951.

[115] P. Valerio *et al.*, "A prototype hybrid pixel detector ASIC for the CLIC experiment," *J. Instrum.*, vol. 9, no. 1, 2014, Art. no. C01012, doi: 10.1088/1748-0221/9/01/C01012.

[116] T. Tick and M. Campbell, "TSV processing of Medipix3 wafers by CEA-LETI: A progress report," *J. Instrum.*, vol. 6, no. 11, 2011, Art. no. C11018, doi: 10.1088/1748-0221/6/11/C11018.

[117] M. Campbell *et al.*, "Towards a new generation of pixel detector readout chips," *J. Instrum.*, vol. 11, no. 1, 2016, Art. no. C01007, doi: 10.1088/1748–0221/11/01/C01007.

[118] P. M. Edic, V. Lobastov, W. Dixon, L. Gjesteby, D. Harrison, and B. Yanoff, "Photon-counting detector for high dose efficiency CT," in *Proc. 5th Work. Med. Appl. Spectroscopy X-Ray Detect. Geneva*, 2019, pp. 8–18.

[119] X. Llopart *et al.*, "Study of low power front-ends for hybrid pixel detectors with sub-NS time tagging," *J. Instrum.*, vol. 14, no. 1, 2019, Art. no. C01024, doi: 10.1088/1748-0221/14/01/C01024.

[120] G. De Geronimo, A. Kandasamy, and P. O'Connor, "Analog peak detector and derandomizer for high-rate spectroscopy," *IEEE Trans. Nucl. Sci.*, vol. 49, no. 4, pp. 1769–1773, Aug. 2002, doi: 10.1109/TNS.2002.801701.

[121] J. P. Rostaing, G. Sicard, A. Dupret, A. Peizerat, and P. Villard, "ADC sampling reduction by an efficient implementation of queue application to X-ray spectrometry imagers," *Electron. Lett.*, vol. 52, no. 6, pp. 428–430, 2016, doi: 10.1049/el.2015.4306.

[122] X. Llopart, "Design and characterization of 64K pixels chips working in single photon processing mode," Ph.D. dissertation, Dept. Comput. Sci., Mid-Sweden Univ., Sundsvall, Sweden, 2007.

[123] M. Campbell *et al.*, "Method for determining a particle and sensor device therefor," U.S. Patent 7 667 205, 2005.

[124] P. Otfinowski and A. Krzyzanowska, "Algorithms for elimination of charge sharing effects in single photon counting pixel detectors," in *Proc. 24th Int. Conf. Mixed Design Integr. Circuits Syst. (MIXDES)*, 2017, pp. 211–214, doi: 10.23919/MIXDES.2017.8005185.

[125] P. O'Connor, "Analog front ends for highly segmented detectors," *Nucl. Instrum. Methods Phys. Res. A Accelerators Spectrometers Detectors Assoc. Equip.*, vol. 522, nos. 1–2, pp. 126–130, 2004, doi: 10.1016/j.nima.2004.01.032.

[126] M. Zuber *et al.*, "An investigation into the temporal stability of CdTe-based photon counting detectors during spectral micro-CT acquisitions," *Biomed. Phys. Eng. Exp.*, vol. 1, no. 2, 2015, Art. no. 025205, doi: 10.1088/2057-1976/1/2/025205.

[127] C. H. M. S. Leng *et al.*, "Photon-counting detector CT: System design and clinical applications of an emerging technology," *Radiographics*, vol. 39, no. 3, pp. 729–743, 2019.